Beryllium melting and erosion on the upper dump plates in JET during three ITER-like wall campaigns

Original
Beryllium melting and erosion on the upper dump plates in JET during three ITER-like wall campaigns / Jepu, I.; Matthews, G. F.; Widdowson, A.; Rubel, M.; Fortuna-Zalena, E.; Zdunek, J.; Petersson, P.; Thompson, V.; Dinca, P.; Porosnicu, C.; Coad, P.; Heinola, K.; Catarino, N.; Pompilian, O. G.; Lungu, C. P.; Subba, F.. - In: NUCLEAR FUSION. - ISSN 0029-5515. - 59:8(2019). [10.1088/1741-4326/ab2076]

Publisher:
IOP PUBLISHING LTD

Published
DOI:10.1088/1741-4326/ab2076

Beryllium melting and erosion on the upper dump plates in JET during three ILW campaigns

I. Jepu[1,2,*], G.F. Matthews[2], A. Widdowson[2], M. Rubel[3], E. Fortuna-Zaleśna[4], J. Zdunek[4],
P. Petersson[3], V. Thompson[2], P. Dinca[1], C. Porosnicu[1], P. Coad[2], K. Heinola[5],
N. Catarino[6], O.G. Pompilian[1], C. P. Lungu[1] and JET Contributors[**]

EUROfusion Consortium, JET, Culham Science Centre, Abingdon, OX14 3DB, UK

[1]*National Institute for Laser Plasma and Radiation Physics, Magurele 077125, Romania*
[2]*CCFE, Culham Science Centre, Abingdon, Oxon, OX14 3DB, UK*
[3]*Royal Institute of Technology (KTH), 10044 Stockholm, Sweden*
[4]*Warsaw University of Technology, 02-507 Warsaw, Poland*
[5]*University of Helsinki, P.O. Box 64, 00560 Helsinki, Finland*
[6]*IPFN, Instituto Superior Técnico, Universidade de Lisboa, Av. Rovisco Pais, 1049-001 Lisboa, Portugal*

Abstract

Data on erosion and melting of beryllium upper limiter tiles, so-called dump plates (DP), are presented for all three campaigns in the JET tokamak with the ITER-like wall. High-resolution images of the upper wall of JET, show clear signs of flash melting on the ridge of the roof-shaped tiles. The melt layers move in the poloidal direction from the inboard to the outboard tile ending on the last DP tile with an upward going waterfall-like melt structure. Melting was caused mainly by unmitigated plasma disruptions. During three ILW campaigns around 15% of all 12376 plasma pulses were catalogued as disruptions. Thermocouple data from the upper dump plates tiles showed a reduction in energy delivered by disruptions with fewer extreme events in the third campaign, ILW-3, in comparison to ILW-1 and ILW-2. The total Be erosion assessed via precision weighing of tiles retrieved from JET during shutdowns indicated the increasing mass loss across campaigns of up to 0.6 g from a single tile. The mass of splashed melted Be on the upper walls was also estimated using the high-resolution images of wall components taken after each campaign. The results agree with the total material loss estimated by tile weighing (~130 g). Morphological and structural analysis performed on Be melt layers revealed a multilayer structure of re-solidified material composed mainly of Be and BeO with some heavy metal impurities Ni, Fe, W. IBA analysis performed across the affected tile ridge in both poloidal and toroidal direction revealed a low D concentration, in the range 1 – 4 x 10^{17} D atoms/cm^2.

Keywords: JET, ITER-Like wall, beryllium, erosion, melt layer motion

PACS: 52.40 Hf

**Corresponding author E-mail:* ionut.jepu@inflpr.ro

[**] See the author list of X. Litaudon et al 2017 Nucl. Fusion 57 102001.

1. Introduction

The main mission of the Joint European Torus (JET) tokamak, the largest operating tokamak in the world [1,2], is to develop operation scenarios and to test fusion technology for next-step devices, especially for ITER. This includes studies of fuel retention and large-scale testing of wall materials. For over twenty years (1985 – 2009) JET was operated with plasma-facing components (PFCs) made predominantly of carbon fibre composites (JET-C) [3]. Since year 1989 some beryllium (Be) components and evaporated layers have constituted a part of the plasma-facing wall programme [3-6]. The choice was motivated by unique physical, chemical and thermo-mechanical properties of Be: low-Z, high thermal conductivity (210 W/mK), oxygen gettering, low neutron activation, compatibility with plasma and vacuum [7].

Implementation of the ITER-Like Wall (JET-ILW) composed of beryllium in the main chamber and tungsten in the divertor was a major step [8-11] on the way to controlling plasma in full metal surrounding and to reduce significantly fuel inventory in comparison to the operation with carbon wall. One of the key aims of the ILW project is to study material erosion, migration, deposition and fuel retention in ITER-relevant scenarios. The research programme with ILW has also been designed to assess lifetime of materials and the impact of metal melting on the operation. The material configuration in JET-ILW is presented in Fig. 1: bulk Be tiles in the main chamber (inner, outer limiters and upper limiters, the latter called dump plates), Be-coated Inconel® tiles in the recessed areas of the inner wall and a mix of bulk W and W-coated carbon fibre composites (W-)CFC tiles in the divertor [8,10]. It should be stressed that positive results obtained in JET-ILW led to a major scientific and technological decision on the ITER divertor materials: to eliminate carbon and to start from Day 1 with only tungsten components [11,12].

In the period 2011 – 2016 three experimental campaigns with deuterium were performed. Each campaign was followed by a major shut-down to allow in-vessel inspection, maintenance, repair or installation of diagnostics and retrieval of selected tiles and wall probes for ex-situ studies. The first ILW campaign (ILW-1, 2011-2012) was focused on the impact of the new wall on plasma operation, material migration and fuel retention [10,13]. During ILW-2 (2013-2014) the operational space was expanded towards high power scenarios while optimising energy confinement and studies of ITER-relevant issues such as disruption mitigation by massive gas injection [14]. The third campaign (ILW-3, 2015-2016) aimed at the increased fusion performance along with integration of all necessary tools such as impurity control and disruption mitigation.

The stepwise increase of the input energy (150 GJ, 201 GJ and 245 GJ in ILW-1 to ILW-3, respectively) and variety of operation scenarios had an impact on the state of the PFCs. This work is concentrated on detailed examination of the upper Dump Plates (DP) following three ILW campaigns. There are several aims for this work: (i) to determine the morphology of tiles addressing also poloidal and toroidal differences; (ii) to relate the melt damage and melt layer propagation to the operation scenarios; (iii) to assess mass losses caused by disruptions and to locate the splashed beryllium on the vessel wall; (iv) to trace and visualize the generation of Be dust during disruptions and (v) to compare the assessed material losses from limiters to the amount of dust collected after the ILW campaigns.

2. Experimental

Each experimental campaign at JET-ILW was followed by a shut-down period when very thorough in-vessel photographic surveys were performed. Also, selected PFCs and wall probes were retrieved for ex-situ analyses and new sets of components and in-vessel diagnostic installed. Both photographic documentation and material analyses have been important elements of the work relevant to analysis of the upper dump plate tiles after each ILW campaign.

The plates are installed in arrays (called beams or ribs) composed of eight individual tiles, as shown in Fig. 2. They are poloidally positioned at the top of the vessel from the inner wall (high field side) towards the outer wall (low field side). In total there are 64 DP beams toroidally positioned around the machine. For clarity of the presentation, individual tiles will be named DP-X, where X is a tile number in the beam: from 1 to 8. High resolution (HR) imaging taken by remote handling allowed for the assessment of PFC conditions and detailed planning of in-vessel activities. Using the survey images, an initial evaluation of the upper DP damage was made. The ***ImageJ*** free software tool [15] was used to map and estimate the amount of Be splashed from the upper DP onto the vessel walls.

Ex-situ studies comprised optical (Leica z16 APO A) and electron (Hitachi, SEM SU-8000) microscopy combined with energy-dispersive X-ray spectroscopy enabling beryllium detection (EDS, Thermo Scientific Ultra Dry, type SDD - silicon drift detector). X- ray diffraction (XRD) was performed using Bruker D8 Discover, detector PSD Vantec1, collimated beam, beam 1.5 mm, of cobalt radiation $K_{\beta 1}$ line (wavelength 0.179 nm); Fe filter was used to discriminate the $K_{\beta 1}$ line. Measurements were done in the 2Θ range from 20 to 130 deg with a step $\Delta 2\Theta$ of 0.05.

Surface composition including deuterium retention was determined along poloidal and toroidal direction across DP-8 and across the Be “waterfall-like” flake using Rutherford backscattering spectroscopy (RBS) and nuclear reaction analysis (NRA). Two surface analysis stations were used: for the measurements across the DP-8 tile, the 2.5 MV Van de Graaff accelerator at Instituto Superior Técnico in Lisbon was used where elemental profiles were measured using the EBS technique, performed with 2.3 MeV proton energy and NRA with $^{3}He^{+}$ ion beams in order to evaluate the retained D amount via the D(3He,p)4He nuclear reaction [16]. Analysis of the Be flake was performed in Sweden using a 3 MeV $^{3}He^{+}$ beam delivered by a 5 MeV tandem accelerator [17].

The analyses have been concentrated on the upper DP-1 to 5 and DP-8. Results are presented for tiles exposed either during single individual ILW campaigns (DP-2 and DP-4) or removed after all three ILW campaigns (2010-2016). Also the study of a Be melt structure (called “Be waterfall-like”) removed from DP-8 has been a part of the analysis plan.

3. Beryllium melting on the Upper Dump Plates

The appearance of the dump plates after three consecutive ILW campaigns is presented in Fig. 3a-1-3, while images in Fig. 3b show toroidal differences recorded after ILW-1 only. It is perceived in Fig. 3a-1 that after the first ILW campaign melting occurred poloidally on the top ridge of each of the tiles predominantly towards the low field side tiles DP-7 and DP-8. Plasma damage was seen also on the high field side, mostly on DP-2 to DP-4. Signs of Be melting was detected on tiles of all 64 DP beams, though there were some toroidal differences suggesting more damage in some octants than in the others. As it can be seen in images of Fig. 3b the melt damage pattern is similar poloidally in each of the three selected positions (Octant 2, 5 and 8) but not toroidally symmetric. A possible cause may be related to the octant-to-octant dump plate misalignments.

After the following two ILW campaigns, this variation was less obvious and melting of the upper DP was considered to be fairly uniform toroidally. After the ILW-2 campaign, an increase of the melt damage was observed on all upper DP, across the chamber. The most affected tile due to melting was found to be DP-8, i.e. the outermost on the low field side, see Fig. 3a-2. The melt layers appear to move in the poloidal direction from the inboard to outboard tile, ending on the last tile with an upwards going waterfall-like melt structure. This melt motion behaviour was previously observed in JET [18-19] and in experiments with tungsten test limiters in TEXTOR [20].

After the ILW-3 campaign similar melting features were observed on all DP plates poloidally distributed (Fig. 3a-3) along each beam and toroidally around the vessel. The most affected areas were those closest to the plasma, i.e. tile ridges, especially on tiles DP-7 and DP-8, culminating in a Be "waterfall" structure at the end of DP-8. Analysis of melting in Section 4 suggest that this originated in ILW-2 and did not get significantly worse in ILW-3. The analyses of Be "waterfall" melt structure removed from one of the dump plates (DP-8), after all three campaigns, is presented in Section 5 of this paper.

3.1 Beryllium mass loss via tile weighing

As mentioned previously, during each shutdown several tiles from the upper dump plate were removed and replaced with new ones. The location from which tiles were removed was in Octant 2: Tile DP-2 and 4. Their appearance shown in Fig. 4 a-c reveals the extent of melt damage after consecutive operation periods. During ILW-1 (Fig. 4a) DP-4 was more affected than DP-2 and a similar damage pattern was found after the ILW-2 campaign (Fig. 4b). Tile DP-4 was also damaged during ILW-3, but no melting was detected on DP-2, as can be inferred from Fig. 4c. There is considerably more melting on DP-4 after ILW-3 than after previous campaigns, but this occurs locally, i.e. it is not poloidally distributed along the ridge of the entire tile. The origin of this damage is attributed to experiments related to runaway electron (RE) generation and mitigation [18].

The mass change (loss or gain) of tiles each ILW-2 and ILW-3 campaigns was determined by high precision weighing. In addition to the above described DP Tiles 2 and 4, the weighing exercise was extended to Tiles 1, 3 and 5 of the same DP beam in Octant 2 for a better estimation of the material balance. No tile weighing was performed initially in 2011 for the unexposed tiles and, therefore, no data is provided for the ILW-1 campaign. Results of the tile weighing are presented in Table 1 for ILW-2 and in Table 2 for the ILW-3 campaign.

The mass loss distribution shows a considerable change in mass for DP-2 during ILW-2 campaign with a total loss of 1.06 g Be, for the individually weighed tiles as compared with the initial mass. It is 15 times more material lost in comparison to that lost from DP-4. The visual inspection of DP damage in Fig. 4b however suggests more melting on DP-4 than on DP-2 but the overall mass change is different, which – in turn indicates that the melting region on DP-4 remained on the tile, without getting the chance to be moved and splashed off the tile. Similar mass loss behaviour was found after ILW-3 campaign on DP-5 of the upper DP but with a relatively smaller value when compared to DP-2 in ILW-2. The plot in Fig. 5 shows a comparison between the mass loss in ILW-2 and ILW-3 campaigns. The tile weighing exercise, shows no specific trend when the mass loss from respective tiles is compared, i.e. DP-2 lost more than DP-5 in ILW-2 but the situation in ILW-3 was opposite. Moreover, it is fair to say that the lack of uniformity in the mass loss distribution across the DP beam implies the impact of individual events causing the mass loss due to melting or erosion, rather than the continuous mass reduction due to normal operation of the reactor. If the masses of individual tiles, referred in Tables 1 and 2, are extrapolated to all 64 DP beams in JET, the overall mass loss would be assessed at the level of around 129.0 g after ILW-2 and approximately 55.3 g after ILW-3. The main reason for this mass loss distribution during campaigns is related to the way JET was operated during the ILW-2 campaign when the focus was on higher power scenarios and ITER-relevant studies on disruption mitigation by massive gas injection. Nevertheless, despite the efforts to control the plasma disruptions by gas injection, most of the melting on the upper dump plates occurred in ILW-2. A closer look into the reasons for Be melting on the upper DPs, mainly occurring during the ILW-2 campaign is presented in Section 4.

3.2 Beryllium mass loss via wall splash estimation

In-vessel high resolution imaging after each ILW campaign showed signs of plasma interaction with PFC in the divertor and main chamber [21-22]. Also, the upper part of the vessel was affected with signs of Be melting and splashing from the upper DPs. This melting resulted in the generation of Be droplets falling from the upper DP into the divertor region as shown in Section 4. In addition, a significant amount of Be was sprayed on to the vacuum vessel wall at the top of the machine towards the outer wall. This feature, initially seen after ILW-1 with a few visible droplets on the walls [13], significantly increased during ILW-2, while after the third campaign it was hard to estimate how much more Be splash had occurred. By analysing the in vessel high resolution images, the amount of Be splashed on the upper part of the vessel was estimated. For this purpose, images taken from the same location in the vessel after each of the campaigns were used to estimate the amount of beryllium deposited on the walls. Using the ImageJ free software tool, a series of droplet maps were created. In Fig. 6 a typical image taken after the third ILW campaign is shown. The region of study is represented by the solid white rectangle which takes into consideration two of the 64 upper DP tile beams present in JET. Yellow dotted rectangles represent the mapping performed to identify Be droplets found in the near vicinity of DP-8. The light green rectangle highlights an actual area where droplets were counted using the ImageJ software. A limitation of this counting and determination of the area of each particle technique is in the resolution of the available image. The pixel calibration was achieved using the known dimension of a Be castellation in DP tile 8, resulting in the number of 6 pixels/mm. A series of assumptions were made to estimate the mass of Be splashed onto the walls. First, all counted particles were considered to be pure Be, with a mass density of 1.85 g/cm^3. Each area given from the particle counting was transposed into the volume by assuming that each surface is in fact the cross-section of a Be sphere. Using these suppositions, the Be mass splashed on the upper outer wall was estimated at the level of ~20 g after ILW-1. For the ILW-2 campaign, the in-vessel image contained also the droplets already counted in ILW-1. Therefore, the mass from ILW-1 was subtracted from the total found after ILW-2 giving~134 g for ILW-2 only. The amount related to ILW-3 assessed using the same approach was~30 g. Data in Table 3 show a comparison made between the Be mass loss recorded via precision tile weighing and the estimation of mass based on in vessel imaging. The values in the table represent the extrapolation made for all the 64 beams of DP tiles on the upper part of JET. It is difficult to assess the error in the count based on splash studies because no sample could be taken for ex-situ analyses. However, the plot in Fig. 7 inform that the estimated mass of Be splashed on the walls has the same trend and similar values to the mass loss recorded by physical weighing of the tiles. Nevertheless, if one takes into consideration the Be splashes thickness of 0.4 and 0.8 μm [23] and assumes that all particles counted on the upper wall are splashes with the maximum thickness of 0.8 μm, the lower limit of the estimated Be mass on the upper wall is around of 200 mg for ILW-2. Overall, it is ~660 times less than determined by weight loss measurement.

4. The origin of the beryllium “waterfall” structure

4.1 Disruptions

Functionality of the next generation fusion tokamak reactors, such as ITER, may be strongly influenced by plasma disruptions. A disruption is characterized by a fast time scale loss of plasma energy and slower loss of plasma current and its associated magnetic energy. This results in a massive heat load and high electromagnetic forces [24-25]. As a consequence, disruption sequences impact on PFCs and mitigation methods remain a critical field of research [26-28].

From the early stage of JET operation in the ILW configuration, namely in year 2011 when the upgrade took place to the PFCs foreseen for the ITER operation, an increase of the disruption rate was noticed, as compared with the carbon wall era. Overall, during JET-C operation, the un-intentional disruption rate dropped to 3.4% between 1984 – 2009 mainly due to steadily improved technical capabilities of machine operation [26, 29]. During all three campaigns with ILW, a total number of 12374 pulses were performed, with 8176 of them exceeding a current of 0.8 MA and a 2 s duration. Out of these, 14% of them were identified and catalogued as un-intended disruptions [30], with most of them moving upwards and inwards, interacting mainly with the upper DP. Melting of the upper DP was noticed in the early stages of ILW-1 campaign which constrained the maximum limit of the plasma current for operation without the protection system being enabled [9, 18]. In conjunction with a frequent use of the massive gas injection (MGI) system for disruption mitigation, ILW-2 campaign was characterized by an increase in the disruption rate to 17% (related to dedicated experiments with MGI), while in ILW-3 a decrease in the frequency of the disruption events was achieved. One can note that the maximum damage on the upper DP was mainly produced during ILW-2. For this reason, the following section focuses mainly on the formation of the Be "waterfall" structure during the second ILW campaign and the most probable pulses that triggered this structure formation.

4.2 Evolution of melting at the upper dump plate

Melt damage on the upper DP due to disruptions was reported after ILW-1 campaign, but a significant increase in the melting behaviour was reported after the ILW-2 campaign [18].

Using the In-Vessel Inspection System (IVIS) cameras, a series of images were taken during ILW-2 to inspect the melting damage on the upper DPs as well as other areas inside JET.

Fig. 8 shows the chronological evolution of the DP-8. It can be seen that the Be "waterfall" structure was gradually formed during several specific disruption events. The damage was observed toroidally on all 64 DPs beams with the flake formation at the low field side at the edge of DP-8. Moreover, melting was observed in the poloidal direction as well, for each of the Be DP beams, starting from the high field side on the inner side of the vessel, namely on DP-1 towards DP-8. Be melting and liquid movement in the poloidal direction was previously reported in JET [18, 19] and similar behaviour was observed for W melting and layer propagation in TEXTOR tokamak [20]. The results indicate that $\boldsymbol{j} \times \mathbf{B}$ force drives the melt layer along the surface. In the case of TEXTOR experiments, the melted W layer moves perpendicularly to the magnetic field in the direction of $\boldsymbol{j} \times \mathbf{B}$, with the main component of the current coming from the thermal electron emission. Calculations show that a thermal emission current density of 1.2 M A/m^2 can account the W melt motion in TEXTOR experiment [20], whereas in JET, for the Be case in studies done for the inner and outer limiter tiles, the estimated current density flowing into a liquid Be surface $\boldsymbol{j}_{\perp} > \boldsymbol{\rho g/B}$, needs to be greater than 6 kA/m^2 for inner limiters to explain the upward movement of the melted layer in the poloidal direction [19]. In the case of upper DP melting, the movement of the melt layer which is driven perpendicular to $\boldsymbol{B}$, is along the surface of the tile in the poloidal direction towards the end of the DPs ribs, on the low field side. This is also due to $\boldsymbol{j} \times \mathbf{B}$ forces, but it is the halo current which is believed to provide the dominant current source [18]. The halo current could provide ~ 100 kA/m^2 of plasma current onto the upper DP tiles resulting a force driving the melt layer that is one order of magnitude higher than the gravitational forces acting on the same melted layer. Hence, once the melted layer reaches the end of the DP tile 8, it moves upwards, defying gravity, and Be is sprayed on to the vessel walls, as described in section 2.2. A schematic representation of the forces acting on the melted Be layer coming from the upper DP-8 is illustrated in Fig. 9, a reprint from the work performed by G. Matthews et al. in [18]. A more detailed explanation of how the melt layer on the upper DP travels poloidally is presented in [18].

From the IVIS images shown in Fig. 8, three main time intervals were identified for the formation and evolution of the Be “waterfall” melt structure at the edge of DP tile 8 during ILW 2 campaign. The first-time interval for which melting started to occur was between pulses 84408 – 84950. Further increase of the melt structure was seen between pulse numbers 84950 – 85257 while the most significant change in the evolution of the melt structure was between pulses 85386 – 87507. It is stressed that for this research, only the validated disruption pulses were taken into consideration to identify as closely as possible the pulses triggering the formation of the Be melt waterfall structure. During ILW-2, 4148 pulses were performed and around 17% of them were catalogued as disruptions, summing intentional and unintentional events. To narrow down the pulse intervals during which melting evolved at the upper DP, thermocouple (TC) data poloidally distributed across DP beam along with infrared camera (IR) imaging were used to confirm melting. Based on the combined TC and IR data, 29 pulses were identified as being the major triggers for damage created on the upper DP and highlighted in Table 4. Nevertheless, one should mention that most of these 29 pulses were deliberated intended, with the aim of studying the PFC interaction and machine limitations during a vertical displacement experiment (VDE).

Two of these 29 pulses are selected and presented in this work as examples, namely pulse number 84832 affecting mainly DP tile 8 and pulse number 85171 affecting DP Tiles 3 to 5. Fig. 10-a shows the thermocouple data readings in pulse No. 84832 on the upper DPs in the poloidal direction, starting from the high field side – DP-1 to the low field side region – DP-8 function of time. On the same figure, the temperature evolution determined during the same pulse using the wide angle view infrared camera (KL7) in Octant 8 is given. The camera views Octants 1 and 2 with a region of interest (ROI) at the upper DPs. As it can be seen in Fig. 10, there is a clear correlation between the two temperature reading techniques. For the IR camera the maximum temperature (950 ^{0}C) is recorded exactly at the moment of the disruption, whereas the TC feedback readings are delayed with the maximum temperature being reached 1.5 s after the actual disruption and the reported temperature being lower than the IR camera. The delay in TC response and lower temperature readings are due to the positioning of the thermocouple, which is 5 mm below the top surface of each tile and is discussed in Section 4.3. Nevertheless, for this pulse, the maximum temperature reading via the TC is up to 225 ^{0}C on DP-8, and considerably lower for the other TCs in the DP tile beam. One important aspect about the disruption during this pulse, is that it affects mainly DP-8, contributing to the Be flake growth on the edge of it. As a confirmation of this statement, Fig. 10-b shows the EFIT plasma equilibrium reconstruction [31] before the disruption presented in blue and at the moment when the disruption is triggered, highlighted in red. Although EFIT reconstructions are more uncertain during disruptions due to reduced currents in the PFCs, there is a strong correlation between the TC data, IR camera data and EFIT plasma reconstructions. In all three cases the most affected tiles are the upper DP-8. Fig. 11 shows a frame sequence capturing the disruption event, recorded by one of the IR cameras. The temperature rises to the maximum in just 0.04 s which is followed by a fast cooling to ~500 ^{0}C. The temperature rise results in melting and droplets falling from the upper DP-8, indicated at 52.26 s and 52.36 s in Fig. 11. Despite the fact that the maximum temperature read by the IR camera is about 950 ^{0}C, i.e. still below the Be melting point of 1287 ^{0}C, the droplet formation and falling from the top of the JET vessel into the divertor region suggest that during the disruption event the actual temperature reached is higher than the Be melting point. This observation is valid for all disruption pulses summarised in Table 4. The second example is a disruption pulse 85171 affecting mainly Tiles 3 to 6 at the upper DP. Fig. 12-a shows the temporal temperature evolution obtained by the wide IR camera (upper plot of the graph) and the temperature fluctuations recorded by the thermocouples in each of the DP (lower plot). The same behaviour as for the previous example, is observed: on the IR camera the response to the temperature increase is fast while the TC response is delayed. Fig. 12-b shows the absolute temperature increase from TC data for each of the DPs. The increase in temperature of DP-3 and DP-4 is 18 to 22 ^{0}C which is between ~9.5% to 12.2% of the pre-disruption values. The EFIT plasma reconstruction position at the moment of the disruption is presented in Fig. 12-c. It shows that the most affected tiles are in the region 3 to 6 which is consistent with the temperature increase determined by thermocouples. For this pulse, the maximum surface temperature from IR camera measurements is ~890 ^{0}C and the TCs' maximum temperature recording is ~205 ^{0}C for DP-6, which is below the melting point of Be. However, there is a good agreement between TC data, IR camera data and EFIT plasma reconstruction positioning which can be seen both on Figs. 10 and 12. Despite the apparent small increase of the temperature readings by the TCs, melting at the top surface does occur. The thermal response of TCs is discussed in Section 4.3.

Using TC readings across the upper DP beam, the tile energy distribution was calculated for pulses listed in Table 4. Two situations were taken into consideration: the case of the DP middle region affected tiles, namely DPs 3 to 6 – which is highlighted in Fig. 13-a, and DP-8 damage which is shown in Fig. 13-b. The plotted energy distributions in Fig.13 are function of tile position across poloidal direction from the high field side of the inner wall towards the low field side of the outer wall. Based on the energy distributions in Fig. 13, there is a clear indication that whenever the disruption occurs and moves upwards there are only one or two possible affected regions, either the central part of the DP tiles (Fig.13-a), or DP-8 at the far end (Fig.13-b). If in a disruption event the plasma discharge moves towards the inner upper side, all the DP tiles are affected, with a predisposition of higher damage on the central ones. One can assume that during these types of events, surface melting occurs, and moreover, the melt Be layer starts to move towards the outer side of the vessel as shown in [18]. Alternatively, if the plasma discharge moves towards upper outer wall, the affected tile is mainly DP-8.

Fig. 13-b shows the energy distribution on all tiles of the DP beam, for the pulses in which the plasma moves towards DP-8. One can notice a higher value for the calculated energy on this far end tile as compared with the lower values on the central tiles. Moreover, these particular pulses result in Be “rain” phenomena from the upper DP (see Fig.11), which indicates that energy loads above 1.2 MJ on cause serious melting leading to droplet formation. The presented energy load values as seen in Fig.13 were calculated for one individual DP beam and extrapolated for the entire JET vessel, summing 64 DP beams. Nevertheless, these high energy loads were only caused from a limited number of disruption events during ILW-2 campaign.

Fig.14 shows a comparison of the energy distribution on all tiles of the upper DP beam, for each ILW campaign. The three plots combine the calculated energy distribution across poloidal direction on the upper DP for only the case of the confirmed and validated disruption events. As it can be seen, there is an overall trend for the central tiles of the upper DP to be affected by the disruptions. Overall, there is a decrease in the energy load on the central tiles from ILW-1 to ILW-2 and ILW-3. One can also notice that upper DP-8 had energy loads above 1.1 MJ mostly during ILW-2. It suggests again that the heavy damage on DP-8 was mainly produced in the second campaign. One important aspect in this reduction in energy delivered by disruptions was the MGI system used at a different threshold during ILW-3 as compared with ILW-2.

4.3 Surface melting modelling

As presented in Section 3.2, there is a discrepancy between the temperature measured by TC inserted into dump plates, the temperature assessed using the IR imaging system and actual events of tile melting. Although the TCs and IR temperature readings follow the same trend, the reported temperature values are lower than the melting point of Be, 1287 ^{0}C, despite the fact that IR cameras imaging showing Be rain (see Fig. 11) and *ex-situ* studies of the retrieved tiles have confirmed melting of their surfaces.

In the following section the analysis of the thermocouple's response to short duration surface heating which potentially cause melting is presented using the plasma heating model shown in Fig.15. Two DP TCs are located 5 mm below the surface: TC-1 in the castellation at the tip of the dump plate and TC-2 in the side castellation as shown. As the plasma heating is close to the toroidal direction, the castellation at the tip of the tile where TC 1 is located is heated from only one side; whereas the side castellation, where TC 2 is located receives full heating (assuming that it is not shaded by adjacent upstream tiles). These two heating regimes are shown in the simplified model in Fig. 16. The castellations on the upstream face receive heating across their full width and can be approximated by the symmetrical heating case shown in Fig. 16-a. This situation can be reasonably modelled using surface heating for a semi-infinite plane, because of the short heating time and the position of the TC nested within the castellation. The castellation at the tip will be heated from only one side and this can be approximated by the asymmetrical case shown in Fig. 16-b. For TC-1 the heating is only on one half of the central castellation, however the penetration depth is less than the castellation depth and, therefore, heating on the adjacent half castellation can be added without affecting the result which is the surface temperature at point A. The short duration of the heat input (<0.1 sec) is much shorter than the penetration time for heat to diffuse to the back of the castellation (> 1 sec) so the solution for 1D heat conduction into a semi-infinite slab under uniform surface heating, given in Equation (1), can be used to estimate the temperature at the TC position. This solution can be applied directly for the symmetrical case as the castellation slits cause the heat to flow to be close to 1D:

$$\Delta T_{SSX}(d,t,q,\lambda,\kappa) = \frac{2\cdot q}{\lambda}\cdot\left(\sqrt{\frac{\kappa\cdot t}{\pi}}\cdot exp\left(\frac{-d^2}{4\cdot\kappa\cdot t}\right)-\frac{d}{2}\cdot erfc\left(\frac{d}{2\cdot\sqrt{\kappa\cdot t}}\right)\right) \tag{1}$$

where: “d” is the distance below surface; “t” is the time; “q” is the heat flux, “κ” is the thermal diffusivity and “λ” is the thermal conductivity. In the asymmetrical case, the solution of the mid plane can be considered as the superposition of the case shown in Fig. 16-b and its mirror image. Hence the solution in this case can be reasonably approximated by halving the result from Equation (1). Figure 17 shows the results in terms of the TC responses for a rectangular heat input of variable duration that just reaches surface melting. For ELM-type heating the duration is typically < 0.01 s and the temperature rise of the TCs located in the ridge of the tile, where the melting occurs, is 20-30 ^{0}C which is consistent with the observations described in Section 4.2

5. Morphological, structural analysis and fuel inventory on DP-8 melt structure

5.1 Optical microscopy

Images in Fig. 18 show the melt damage on DP-8: (a) the general view of the molten area, (b) the Be flake detached from the side of the tile and – on (c) and (d) the flake structure flake structure recorded with 3D optical microscope. Gap bridging between castellations along the poloidal direction is also noticed. The bridging was reported already earlier in [18-20], but the current work brings also a view in between the castellations and shows (in Fig. 19) how deep the molten Be penetrated into the groves. This analysis was performed after DP-8 was cut both on poloidal and toroidal direction [32]. One can notice that the bridging is not limited to the surface region of the tile, the grooves of castellation are being partially filled with molten Be. Moreover, the filling is not uniform across toroidal distribution and it does not reveal any systematic trend, as the gaps are partly filled with molten Be at a range of depths, from 0.2 mm to 3.5 mm. Nevertheless, neither toroidal or poloidal grooves were fully filled with molten Be. The maximum depth filled is estimated at 30% of the whole depth. Once the melt layer has reached the edge of the tile, it further moves upwards to the top of the vessel forming a gravity-defying waterfall-like structure of a complex shape, as shown in Fig. 18 (b). In close-up images of the top surface, in Fig. 18 (c, d), one perceives numerous Be droplets ranging in size (diameter) from micro-to millimetres. Microscopy data provide a clear evidence of multiple melting and cooling cycles which led to material losses from the plasma-facing side of the dump plate tile, summing 129 g of Be lost from the upper DPs during the ILW-2 campaign and 55 g of lost material during ILW-3, as presented in Section 3.1, and the formation of layers. Fig. 20 shows the bottom part of the flake revealing its complex multi-layer structure. In the entire flake one can notice a few main layers which clearly indicate that their formation was linked with several high-power events during the ILW campaigns, most probably associated with disruptions during the ILW-2 operation. The thickness of the sub-layers range from 60 to 500 µm.

5.2 Topography and surface composition

Comprehensive analyses of the surface morphology were performed on both sides of the flake: (a) the top one on the plasma-facing side, thus having the last (the "newest") melt layer; (b) the bottom facing the limiter side surface which corresponds to the first (the "oldest") formed layer; due to its positioning it can be considered as plasma-shadowed layer. Secondary electron images (SEI) of the top surface, shown in Fig. 21 (a, b), reveal a complex topography and multilayer structure with droplets. X-ray spectra in Fig. 21 (c, d) provide evidence on the composition of two consecutive strata: the very top one and the next. Both contain not only beryllium and oxygen (O from plasma impurity gettering and in-air oxidation), but also C, N, Fe, Ni and W thus proving the deposition of those impurity species from the plasma. One should stress that the recorded Be feature in the X-ray spectra is small because Be K_α radiation has low energy (108 eV) and it is attenuated by any co-deposit present on the surface of the studied material. The main difference between the layers is in the content of medium- and high-Z metals, which is greater in the deeper layer. This indicates that the layers were formed in different events. The spectra also indicate that Be was coated by co-deposit before the next (upper layer) was formed. As a consequence, the layers were exposed to plasma (and corresponding deposition processes) for different periods of time. SEM images in Fig. 22 (a-c) demonstrate splitting of the main Be layers into a large number of sublayers of less than 1 µm in thickness. The sublayers also tend to split forming 20-30 nm strata. The structure of the multiple strata is similar to C-rich co-deposits found in the carbon wall machines, e.g. TEXTOR and Tore Supra [33]. One could expect this type of surface to be potentially a significant source of fine Be dust if such features are toroidally distributed on all 64 beams of DP tiles with enhanced melting on each DP 8. Additional features of the melt layer are shown in Fig. 23: the formation of droplets and the ripples or – in other words – capillary waves (indicated by an arrow) which suggest material motion (rotation) during the beryllium re-solidification.

Features of the back side of the flake facing the limiter surface are shown in Fig. 24 (a-b). Backscattered electron image (BEI) and EDX spectrum, shown respectively in Fig. 24 (b) and (c), point out that beryllium is the main element. There are no metallic impurities and even the oxygen signal is moderate thus indicating that no in-vessel oxidation and co-deposition took place on that surface. This means tight adherence of the flake to the side wall of the DP tile. In some areas one could find perpendicular cracks, as marked by arrows in Fig. 24 (d). This suggests strong internal stress which leads to splitting of the re-solidified material.

5.3 Crystallographic structure of the re-solidified material

X-ray diffraction was performed on both sides of the flake to obtain insight into the chemical composition and crystalline nature of it. Spectra in Fig. 25 (a and b) show results obtained in four different areas. Point 1 and 2 represent measurements performed on the backside of the Be flake which corresponds to the oldest Be layers formed during first disruption pulses. Data in Points 3 and 4 are for the front side of the flake which represents the formation of the “newest” layers. The measurements were performed between 40^o and 110^o in Bragg-Bretano configuration. All diffraction patterns reveal the textured crystalline nature of the measured zones on both backside and frontside of the sample evidenced by the presence of 3 main crystalline phases accounted in the composition. By far the most dominant crystalline phase corresponds to a Be metallic phase, belonging to the $P6_3$ mmc/ (194) space group, with a hexagonal closed-packed structure atom arrangement in the elemental cell. The existence of the above-mentioned phase is confirmed by the oriented growth of the crystallites on Be (100), Be (002), Be (101), Be (110), and Be (112) planes with preferential crystalline orientations on Be (101) plane.

A variation in the intensity of the Be (002) orientation in relation to the other orientations corresponding to Be metallic phase were observed for all measured points which reveals the non-homogenous crystalline nature of the Be waterfall flake. The crystallite dimensions were estimated from the diffractograms using the Scherer equation. This analysis was conducted only for the most intense orientations of the Be metallic phase, namely Be (101). The results confirm the nano-dimension of the crystallites with a measured range between 21.5 nm in Point 4 to 28.4 nm in Point 2.

The presence of beryllium oxide in the analysed flake derives from the fact that Be acts as an oxygen getter. The oxide phase has a normal adamant structure, bromellite (BeO) with $P6_3$ mc (186) space group is evidenced by the presence of three minor peaks centered roughly at 44.8^o, 48.3^o and 51.4^o belonging to X-ray reflection from BeO (100), BeO (002) and BeO (101). There is no difference in the relative intensities of the BeO peaks between the backside and frontside diffraction patterns. The identification of a third crystalline phase based on reflections at 53.6^o, 84.6^o and 93.6^o has been proven very difficult due to the range of compounds that can be formed between Be and trace of metallic impurities present in the surface region: W, Ni, Cr, Fe. There is still a degree of uncertainty, but the best match was the intermetallic crystalline phase $Be_{22}W$ Fd 3m (227) space group with 711, 664 and 10 4 2 diffraction planes, more clearly shown in Fig.25-b. This intermetallic compound can be formed as a result of low concentrations of tungsten from the divertor or some main chamber surfaces onto the Be surface at temperatures in excess of 900 ^oC. Indeed, the presence of tungsten was found elsewhere on the main chamber surfaces [22]. The most prominent peaks were observed for Points 3 and 4, i.e. on the front side of the flake and these data are sustained also by the EDX measurements which identified a higher W impurity concentration on the front side in comparison with the back side.

5.4 Deuterium retention

Results of NRA measurements performed on DP-8 are summarised in Fig. 26, where the image (26-a) shows the lines of analysis in the toroidal (Fig. 26 b) and poloidal direction (Fig 26-c). There are some variations in the deuterium content, but the major result is such that the amounts of fuel trapped in the studied dump plate are small: $1 - 4 \times 10^{17}$ cm^{-2}. Such concentrations are considered to be generally low, not only in comparison to JET-C (up to 1×10^{20} cm^{-2} [4,5, 34]) but also to the data for the JET-ILW divertor, D in the 10^{18} cm^{-2} range [35, 36]. It is seen in Fig. 26-b that the maximum D concentrations (up to 4×10^{17} cm^{-2}) are found on both sides of the melt zone. In the melted zone itself the concentration drops by a factor more than two to about 1.7×10^{17} cm^{-2}. Similar amounts of D are measured along the entire melt zone with only some variations ($1.2 - 2.3 \times 10^{17}$ cm^{-2}) along the poloidal direction with a certain increase towards the high field side. However, based on the analysis of a single plate (the only available from this poloidal location for ex-situ studies) it is hard to draw conclusions whether this is a general trend for the other tiles. The results in Fig. 26 indicate that the release of deuterium from the melt zone most probably occurred during the last phase of the ILW-3 operation.

Nuclear reaction analyses on both sides of the flake have yielded data on the deuterium content in the vertical direction, i.e. from the tip of the dump plate towards the top of the machine. The data are shown in Figure 27. On the front side (Fig.27 a-b) the deuterium concentration varies from 6.3×10^{17} cm^{-2} (tip of DP) to 1.1×10^{17} cm^{-2} in the middle part and then starts increasing again. The concentration on the back changes in the narrow range from 6.1×10^{17} cm^{-2} (central part of Be flake) to about 3.7×10^{17} cm^{-2} (tip of Be flake). All these differences and variations, especially on the front side, may be associated with significant non-uniformity in surface topography, as documented by images in Figures 18-20. Such topographical features (dips, cavities, edges etc) may obstruct to some extent the accuracy of

IBA measurements. It does not change the fact that fuel content in the molten flake is low, i.e. below 1×10^{18} cm^{-2}. An important result is that deuterium is only detected in the surface region (1 µm) of the fairly rough flake, while the depth information of NRA with a 3 MeV 3He+ beam in a Be target exceeds the depth of 10 µm.

In summary, all IBA results clearly prove low fuel content on the dump plate, both in the not-damaged and in the re-solidified material. They also indicate that there is no excessive trapping of fuel in the melt zones, as tentatively suggested following the studies of beryllium tiles from the MkI-Be divertor [5].

6. Conclusions

The current work highlights melting and erosion of the upper DP phenomena in JET during all three ILW campaigns, the triggering factors behind it and a complete set of imaging survey, morphological, structural and fuel inventory analysis on the most affected DP tile due to melting. The undisputed reason for melting was the unmitigated disruption events which tend to move the melt layers in the poloidal direction from the inboard to outboard tile ending on the last tile with an upward going waterfall-like melt structure. It is the halo current which is believed to provide the $\boldsymbol{j}\times\boldsymbol{B}$ force that drives the melt layer along the surface. During all three ILW campaigns ~15 % of the total pulses were catalogued as disruption events. The focus of this work was on the ILW-2 disruption events which caused the greatest damage to the upper DP, i.e. their melting, melt layer motion and material splashing, especially during ILW-2. Temperature readings from the thermocouple imbedded into one of the 64 DP beams, correlated with IR camera images were used to identify the main disruption pulses that affected the upper DP. Twentynine pulses were found as the main triggers for the melt damage along the poloidal direction. However, most of these identified pulses were induced disruptions so one can conclude that the actual damage was not random but on purpose made.

Each ILW campaign was followed by retrieval of selected tiles for ex-situ analyses. High precision weighing of selected DP tiles revealed a mass loss of 129 g of Be after the second ILW campaign and 30 g after the third ILW campaign. Unfortunately, no such data were collected after the first ILW campaign because the weight of the first-installed tiles was not measured. High-resolution images taken of the removed DP tiles across poloidal direction revealed consistent melting damage mainly on the top ridge of each of the tiles, with different features after each campaign. Using these high-resolution images, the amount of Be splashed from DP8 on the vessel walls was estimated and the figures were in close concordance with the tile weighing exercise. By comparison, the total mass of dust collected in the divertor area in all three ILW campaigns is in the range of 3.7 g [23, 37-38]. However, Be dust as flakes and droplets represents ~ 30% of the whole collected dust by vacuuming, in the range of 0.52 g for ILW-2 [23]. Extrapolating this result to all three campaigns, the amount of Be dust found in the divertor area as dust is estimated to be ~ 160 times less than the mass of Be lost from the upper DP and deposited onto the vessel wall. This is an indication that most of the Be splashed from the upper DP ended primary on the vessel walls and does not contribute significantly to dust and droplet formation in the divertor region.

Energy loads on the DP calculated using the thermocouples in the poloidal direction were consistent with the damage seen on the tiles. There was a decrease in the energy loads on the upper DP central tile (DP-3 to DP-5) during all three campaigns, with significant lower power loads during ILW-3. The energy loads on DP-8 peaked during ILW-2 campaign, where the most damage on the upper DP was reported.

The response of typical DP thermocouples located 5 mm below the tile surface has been analysed by modelling the surface heating of a semi-infinite plane, subject to a short heating pulse representative of ELM-type heating. For a rectangular heat input of short duration, typically < 0.01 s, sufficient for surface melting, the temperature increase at the TC is in the range of 20-30 ^{0}C.

3D optical microscopy on DP-8 along with the Be “waterfall” structure highlighted the amount of damage created on the upper section of JET wall due to disruptions. Melting and movement of the molten Be towards the margin of DP 8 in poloidal displacement was reported. Close attention was paid to the castellation bridging phenomena which was previously seen in [18-20]. In this study we show that bridging is not limited to the surface region of the tile and that castellation gaps are filled with molten Be to depths ranging from 0.2 – 3.5 mm.

Structural and morphological analysis performed on both sides of the Be waterfall flake revealed highly complex multilayer structure with traces of W, Ni, Cr and Fe impurities on the top surface of the flake, and very few impurities on the back side of it. The main difference between the layers is in the content of medium and high-Z metals, which is greater in the deeper layers. The variation in these impurities is a strong indication that the layers were formed over time by different off normal events. SEM images highlight the complexity of the melted layers with the presence of multiple strata within a single main layer, of droplets and of capillary waves which indicate material motion (rotation) during the beryllium re-solidification. X-ray analysis measurements reveal the textured crystalline nature of the measured zones. The most dominant crystalline phase corresponds to a Be metallic phase but there are also traces of BeO and an intermetallic crystalline phase formed between Be and W, namely $Be_{22}W$.

IBA analysis revealed a low D concentration on the melted areas of DP-8, both in toroidal and poloidal direction and an increase D concentration on the areas less affected by the melting phenomena. The high surface temperature during melting is likely to result in the release of trapped D thus explaining the variation between melted and non-melted areas. Similar results were seen on the Be waterfall structure on both front and bottom sides, with D concentrations ranging from 1.1 - 6.3 × 10^{17} cm^{-2}. Overall, the results clearly show low fuel content on the upper dump plate and Be “waterfall” structure which comprise both the non-damaged surfaces and the re-solidified ones, with no excessive trapping of fuel in the melt zones.

To our knowledge, this work is the most comprehensive and detailed study of beryllium erosion and release from the first wall components exposed to fusion plasmas. This holistic approach based on the combination of several material research techniques: correlation of disruption history (triggering factors) with melt events, in vessel IR camera-based survey showing surface heating and material ejected from the upper dump plates, modelling of melt layer migration, and surface analysis techniques to study the migration, composition and fuel retention of the melt layers, has contributed to deepening the insight into the damage of the main vessel components.

Acknowledgements

This work has been carried out within the framework of the EUROfusion Consortium and has received funding from the Euratom research and training programme 2014-2018 and 2019-2020 under grant agreement No 633053. The views and opinions expressed herein do not necessarily reflect those of the European Commission.

References

[1] Keilhacker M *et al* 1999 *J. Nucl. Mater.* **266–269** 1

[2] Litaudon X and JET Contributors, 2017 *Nucl. Fusion* **57** 102001

[3] Thomas PR and JET Team, 1990 *J. Nucl. Mater.* **176-177** 3

[4] Peacock AT and the JET Team, 1990 *J. Nucl. Mater.* **176-177** 326

[5] Coad JP *et al* 1997 *J. Nucl. Mater.* **241-243** 408

[6] Rubel M *et al* 2009 *J. Nucl. Mater.* **386-388** 729

[7] Federici G *et al* 2001 *Nucl. Fusion* **41** 1967

[8] Matthews GF *et al* 2007 *Phys. Scr.* **T128** 137

[9] Matthews GF *et al* 2011 *Phys. Scr.* **T145** 014001

[10] Matthews GF *et al* 2013 *J. Nucl. Mater.* **438** S2.

[11] Brezinsek S *et al* 2015 *J. Nucl. Mater.* **463** 11

[12] Merola M *et al* 2014 *Fusion Eng. Des.* **89** 890

[13] Widdowson A *et al* 2014 *Phys. Scr.* **T159** 014010

[14] Lehnen M *et al* 2011 *Nucl. Fusion* **51** 123010.

[15] https://imagej.nih.gov/ij/

[16] Catarino N*et al* 2017 *Nucl. Mater. Energy* **12** 559

[17] P. Petersson *et al* 2015 *J. Nucl. Mater.* **463** 814

[18] Matthews GF *et al* 2016 *Phys. Scr.* **T167** 014070

[19] Sergienko G *et al* 2014 *Phys. Scr.* **T159** 014041

[20] Sergienko G *et al* 2007 *Phys. Scr.* **T128** 81

[21] Riccardo V *et al* 2013 *Fusion Eng. Des.* **88** 585

[22] Baron-Wiechec A *et al* 2015 *J. Nucl. Mater.* **463** 157

[23] Fortuna-Zalesna E *et al* 2017 *Phys. Scr.* **T170** 014038

[24] Hender TC *et al* 2007 *Nucl. Fusion* **47** S128

[25] de Vries P C *et al* 2012 *Plasma Phys. Control. Fusion* **54** 124032

[26] de Vries P C *et al* 2011 *Nucl. Fusion* **51** 053018

[27] Riccardo V *et al* 2004 *Plasma Phys. Control. Fusion* **46** 925.

[28] Whyte DG *et al* 2002 *Phys. Rev. Lett.* **89** 055001

[29] de Vries P C *et al* 2009 *Nucl. Fusion* **49** 055011

[30] Joffrin E *et al 26th IAEA Fusion Energy Conference* – IAEA CN-234, 2016, EX/9-1,

[31] Brix M *et al* 2008 *Rev. Sci. Instrum.* **79** 10F325.

[32] Widdowson A *et al* 2016 *Phys. Scr.* **T167** (014057)

[33] Ivanova D *et al* 2009 *Phys. Scr.* **T138** 014025

[34] Coad JP *et al* 2018 *Fusion Eng. Des.* **138** 78

[35] Heinola K *et al* 2016 *Phys. Scr*. **T167** 014075

[36] Mayer M *et al* 2016 *Phys. Scr*. **T167** 014051

[37] Widdowson A *et al* 2017 *Nucl. Mater. Energy* **12** 499

[38] Rubel M *et al* 2018 *Fusion Eng. Des.* **136** 579

Table 1. Mass of individual DP tiles before and after ILW 2 campaign

ILW 2 (2012- 2014) tile ID	**2012 in mass (g)**	**2014 out mass (g)**	**2012-2014 Δm (g)**
2BC1	903.9	903.860	-0.040
2BC2	746.16	745.100	-1.060
2BC3	737.87	737.780	-0.090
2BC4	733.98	733.910	-0.070
2BC5	661.4	661.410	0.010

Table 2.

Mass of individual DP tiles before and after ILW 3 campaign

ILW 3 (2014- 2016) tile ID	**2015 in mass (g)**	**2017 out mass (g)**	**2014-2016 Δm (g)**
2BC1	903.880	903.890	0.010
2BC2	745.070	745.070	0.000
2BC3	737.770	737.780	0.010
2BC4	733.570	733.550	-0.020
2BC5	661.410	660.890	-0.520

Table 3. Comparison between mass loss via tile weighing and mass estimation via in vessel image analysis

Campaign	**Overall mass loss by tile weighing (g)**	**Estimated Be mass on upper outer walls via imaging (g)**
ILW 1 (2010 - 2012)	No data	19.067
ILW 2 (2012 - 2014)	129.03	133.741
ILW 3 (2014 - 2016)	55.30	29.925

Table 4. Top 29 triggering pulses for the upper DP damage during ILW2

Pulse no.	**Affected DP tiles**	**Maximum reached temperature (^{0}C) on affected tile via IR camera**	**Pulse description**
84588	8	927	VDE test
84593	5-8	897	VDE test
84594	5-8	964	VDE test
84612	8	976	VDE test
84613	8	907	VDE test
84614	8	915	VDE test
84675	8	1020	VDE
84832	8	1020	VDE
84837	1-4	1016	Deliberate W event/VDE
85171	3-5	890	VDE
85386	4-6	1020	VDE from FRFA trip
85408	3-5	924	Large density discharge
85409	3-5	1020	Large density discharge
85413	3-5	1020	Large density discharge
85414	3-5	1020	"Impurity influx
85430	3-5	1020	Radiative collapse
85434	3-5	1010	Radiative collapse
85801	8	1000	Induced VDE
85803	8	1020	Induced VDE
85804	8	1020	Induced VDE
85805	8	1020	Induced VDE
85806	8	1020	Induced VDE
85807	8	1020	Induced VDE
85857	8	1020	Induced VDE
85858	8	1020	Induced VDE
86793	8	1020	Runaway studies
87296	3-5; 8	1020	VDE
87507	4-8	1020	Minor VDE
87526	3-5, 8	1016	VDE

Figure captions

Figure 1. Schematic representation of JET ILW materials. Main chamber complied of bulk Be (1)in Upper Dump Plates, Inner Wall Guard Limiters, Outer Poloidal Limiters – highlighted and in green colour; Be – coated Inner Wall Cladding (2) highlighted in blue colour and divertor containing W coated CFC components (3) – highlighted in purple colour; pure W (4) highlighted in red colour.

Figure 2. Schematic representation of JET single beam Dump Plates tiles and Mushroom Protection Limiters (MPL). Located at the top of the main chamber, each single beam is formed of 8 individual Be tiles, poloidally positioned from the inner wall towards the outer wall.

Figure 3. a) In vessel images of melting damage on the upper dump plates for the same tile beam located in Octant 6 after the first ILW campaign (3a-1), second ILW campaign (3a-2) and third ILW campaign (3a-3). Increased melting is noticed on the low field side exposed tiles 7 and 8. Be “waterfall” structure present after the ILW 2 campaign. b) In vessel images of melting damage across the upper dump plates after ILW1, with different damage grades based on position (Octant 2, 5 and 8) indicating an un-uniform toroidal melting distribution.

Figure 4. In vessel images of melting on tiles removed for *post-mortem* analysis after ILW 1 (a), ILW 2 (b) and ILW 3(c). Note uniform melting distribution across all tiles, with increase melting features on tile 4 in ILW 1&2 campaigns. Less melting features are seen on same positions after ILW 3.

Figure 5. ILW 2 and ILW 3 mass ls on upper DP comparison. One can notice significant change in the mass of tile 2 during ILW 2 while ILW 3 is characterized by a more considerable mass loss on tile 5. Overall, there is no particular trend in the mass loss pattern across the DP tiles.

Figure 6. In vessel image of the upper DP wall regions after ILW 3 campaign. The interested region is blue short doted, taking into consideration two of the 64 DP beams ends. Yellow rectangles are the particle mapping on the walls while red rectangle shows an actual particle counting region using the ImageJ software.

Figure 7. DP Be mass loss comparison between physical tile weighing highlighted in orange and estimation made via high resolution imaging and particle counting using ImageJ software.

Figure 8. Be “waterfall” melt damage on the upper DP 8 evolution. Images from left to right show the chronological increase of the melt damage during ILW 2. Based on these images, an interval with the most probable triggering events was found.

Figure 9. Reprint of figure 2 in [16] –(a) Schematic showing a current $\boldsymbol{j}_{\perp}$ arriving from the plasma and passing through a liquid Be layer (red) and into the solid Be limiter surface. (b) If the liquid layer leaves the surface, a parallel current $j_{\parallel}$ arises and the resulting $\boldsymbol{j} \times \mathbf{B}$ force pushes back. (c) If a bridge is produced then the opposing $\boldsymbol{j} \times \mathbf{B}$ forces may shear the layer apart

Figure 10. a) Temperature evolution on the upper DP function of time during pulse number 84832 using TC reading (lower side of the graph) and wide view of IR camera (upper side of the graph). There is a good correlation between the temperature rise when the disruption starts for both techniques. TC data offer a delayed feedback while IR camera response is instant. b) EFIT plasma equilibrium reconstruction before the disruption – in blue colour, and at the moment of the disruption – in red colour. There is a clear correlation between the TC data reading on the upper DP, IR camera readings and EFIT reconstruction which indicates that majority of the damage is created on DP 8.

Figure 11. IR wide camera frame sequence showing the evolution of the upper DP temperature during a disruption in pulse number 84832 followed by melting and droplet formation. There is a fast increase of temperature (~200 ^{0}C to 950 ^{0}C in 0.04 s) followed by a fast decrease in the following 0.04 s. Beryllium droplets falling from the upper DP are noticed right after this fast temperature transition. Since the maximum temperature reached is below the Be melting temperature it is clear that the real tile temperature is higher than the camera reading.

Figure 12. a) Temperature evolution on the upper DP function of time during pulse number 85171 using TC reading (lower side of the graph) and the wide view IR camera (upper side of the graph). Similar correlation as in figure 10 are seen, between the TC data and the IR camera temperature readings. b) Absolute temperature increase for each of the DPs. DP 3 and 4 suffer an increase of 18 to 22 ^{0}C which represents a range between ~9.5% to 12.2% temperature modification as compared with the pre-disruption values. c) The EFIT plasma reconstruction position before the disruption – in blue colour, and at the moment of the disruption – in red colour. It is a clear indication that the most affected tiles are somewhere in the region 3 to 6 based on the

temperature increase of each of the thermocouples and the plasma position at the disruption point.

Figure 13. a) DP tile energy distribution function of poloidal displacement of tiles for the pulses in Table 4 affecting mostly central tiles, namely DP 3 to 5. b) DP tile energy distribution for the pulses in Table 4 affecting mostly DP 8.

Figure 14. DP tile energy distribution function of poloidal displacement for all three ILW campaigns. A decrease on the energy distribution affecting central tiles on the upper DP, namely DP 3 to 6 is noticed after each campaign. A considerable decrease on the energy distribution on tile 8 is seen after the ILW 2 as compared to ILW 3 which suggest that melting and heavy damage on the upper DP was mainly caused by singular events in the second ILW campaign.

Figure 15. Thermocouple positions and plasma heating of upper DP tile. Note that each TC is 5 mm below the surface of the tile

Figure 16. Idealised DP castellation heating for *a)* symmetrical and b) asymmetrical case

Figure 17. Predicted TC Response when Surface Reached Melting

Figure 18. a) Melt damage across poloidal direction on upper DP 8, with a close-up on the “waterfall” structure in b); 3D optical microscopy imaging showing complex features of the melted flake itself in c) and melt damage near to the top edge of the tile in d). One can notice the multitude of Be droplets in different shapes and sizes, ranging from microns to millimetres in diameter.

Figure 19. 3D optical microscopy image showing melt damage into the tile castellations. Bridging is observed but not limited to the surface only. The grooves are randomly filled with molten Be reaching depths between 0.2 and 3.5 mm.

Figure 20. 3D optical microscopy image showing the bottom side of the Be “waterfall” multi-layered structure. Several main layers can be noted, with thicknesses ranging from 60 to 500 µm.

Figure 21. Secondary electron images (SEI) of the top surface (a, b), prove a complex topography and multilayer structure with droplets. X-ray spectra in (c, d) provide evidence on the composition of two consecutive strata.

Figure 22. SEM images in (a-c) highlight the presence of multiple strata within a single main layer which is an indication that one main Be layer is split into a large number of sublayers of less than 1 µm in thickness.

Figure 23. SEM image showing the formation of droplets and the ripples or (indicated by an arrow) which suggest material motion (rotation) during the beryllium re-solidification.

Figure 24. Back side of the flake facing the limiter surface are shown in (a). Backscattered electron image (BEI) (c) and EDX spectrum (d) prove beryllium to be the main element. Strong internal stress leading to splitting are shown in (d) as marked by arrows.

Figure 25. a) XRD diffraction patterns performed on two regions of the Be waterfall structure. Point 1 and 2 correspond to the bottom – shadowed side of the flake. Points 3 and 4 correspond to the top side of the flake. All measured reveal the textured crystalline nature of the measured zones. b) The most dominant crystalline phase corresponds to a Be metallic phase but also traces of BeO and intermetallic crystalline phase formed between Be and W, namely $Be_{22}W$

Figure 26. a) IBA analysis performed on DP 8 along poloidal and toroidal direction; b) D concentration along toroidal direction highlights a lower D presence on the melted areas along the top ridge of DP8; c) D concentration along poloidal direction shows a lower D presence across the melted area of DP8 with the lowest values reached where the most damage is achieved, in the low field side of the tile and where the Be waterfall structure is generated

Figure 27. a-b) D concentration along poloidal direction on the front side of the Be waterfall structure and c-d) on the bottom side. D concentration values are ranging from $1.1 - 6.3 \times 10^{17}$ cm^{-2} on both exposed and shadowed surfaces, the differences being associated with the non-uniformity of the surface.

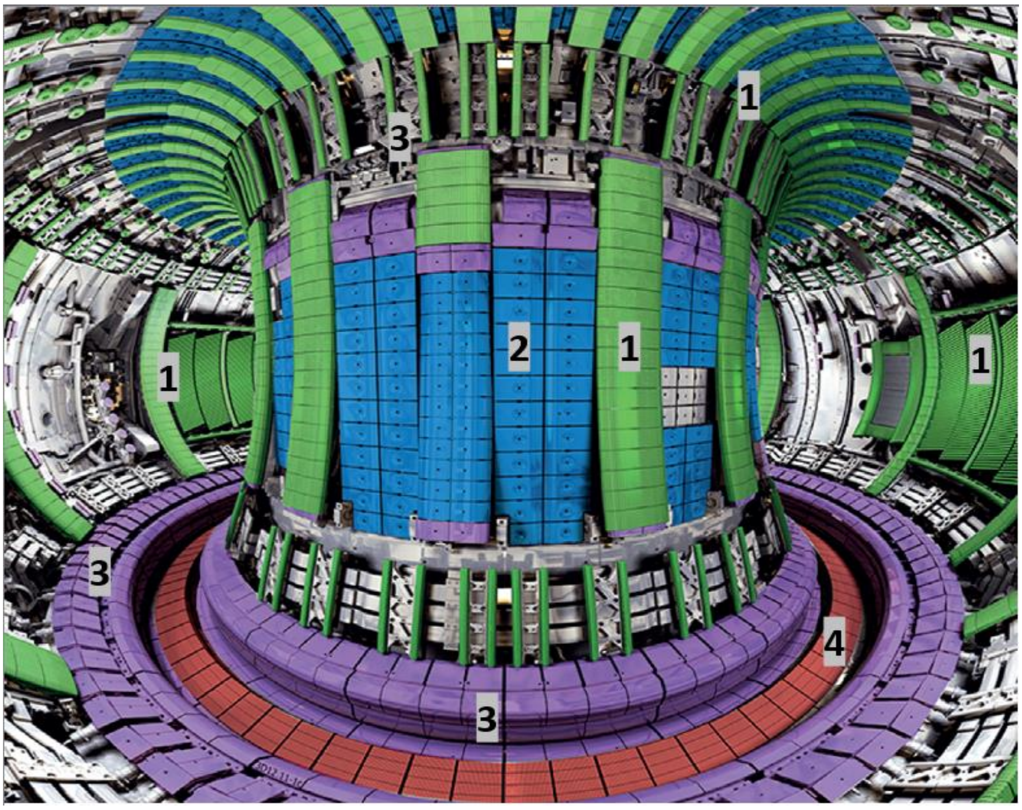

Figure 1

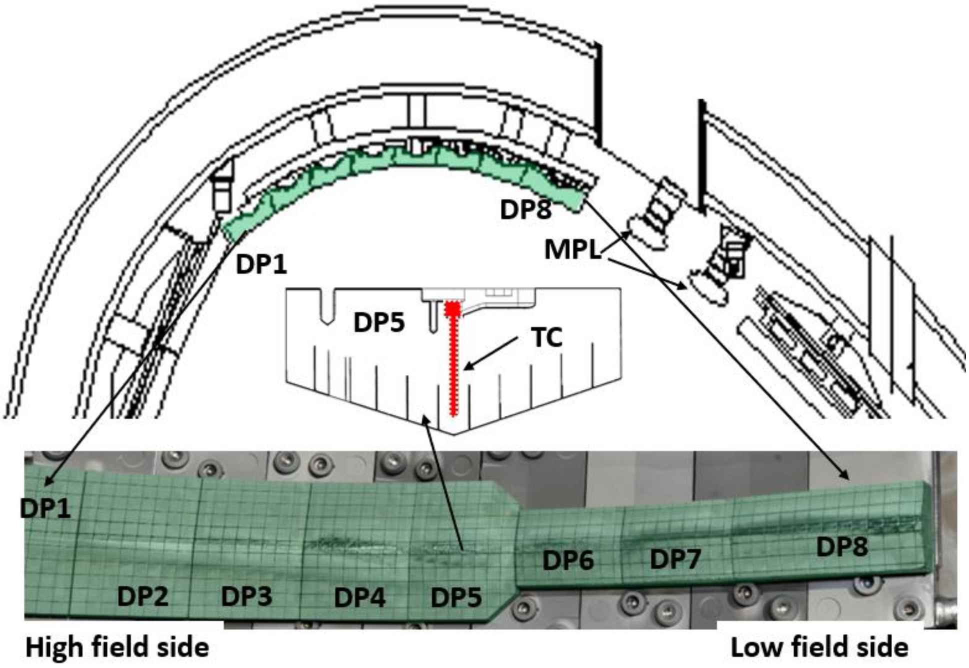

Figure 2

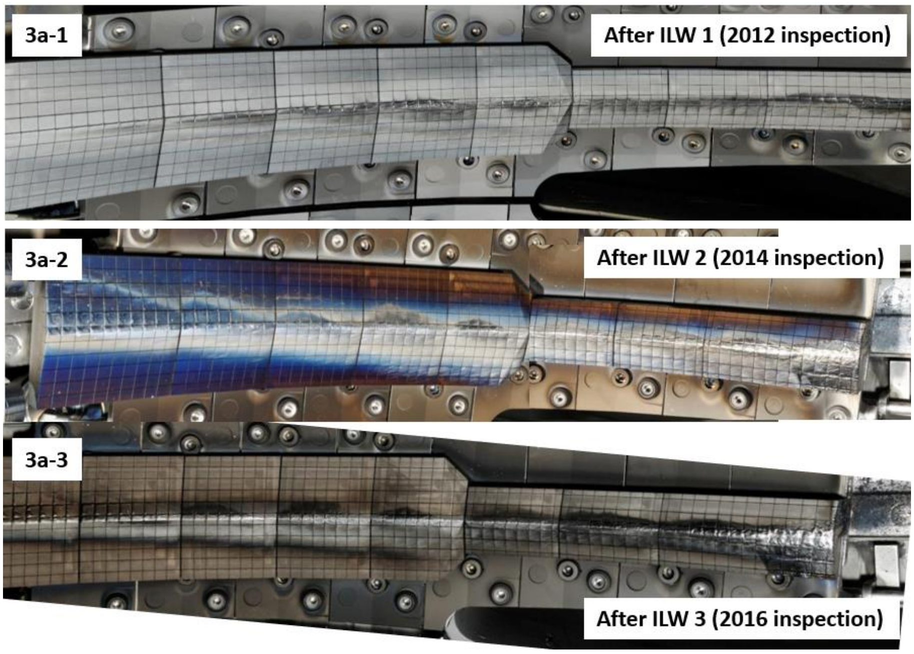

Figure 3 a

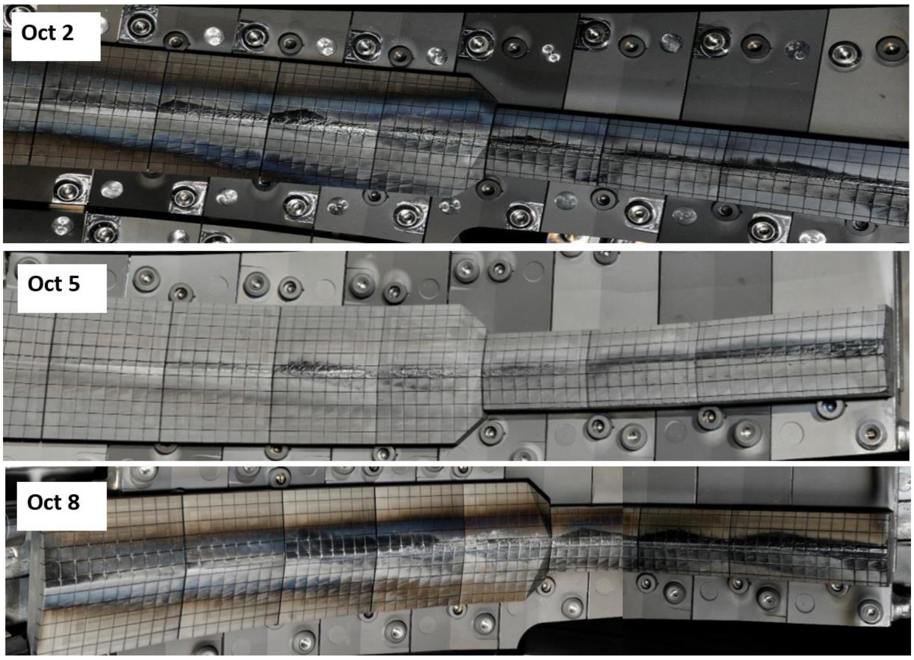

Figure 3 b

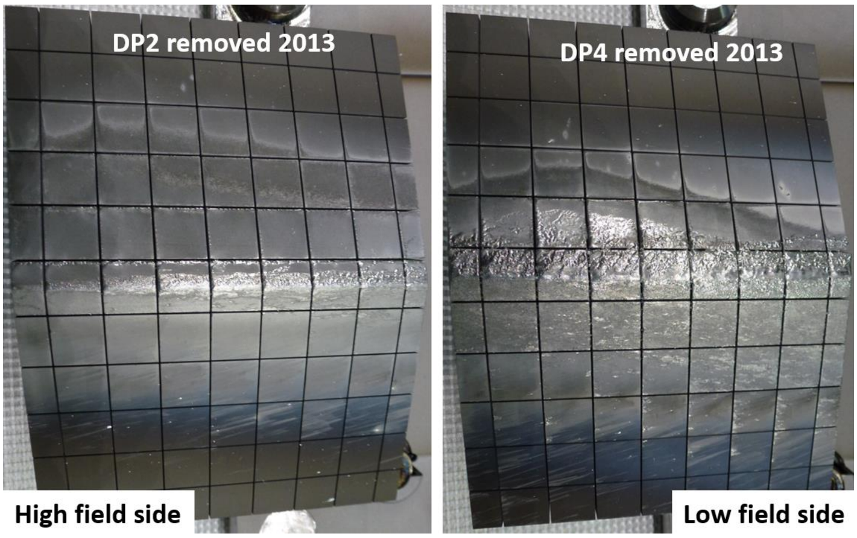

Figure 4 a

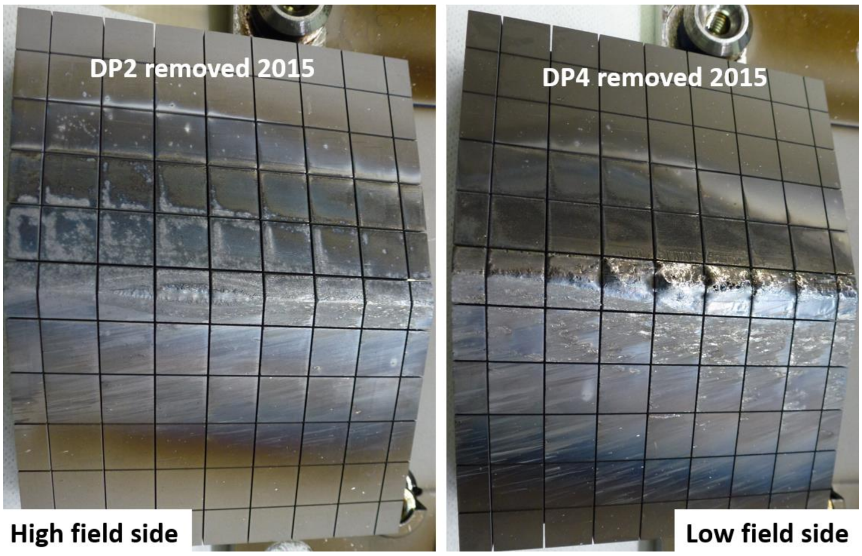

Figure 4 b

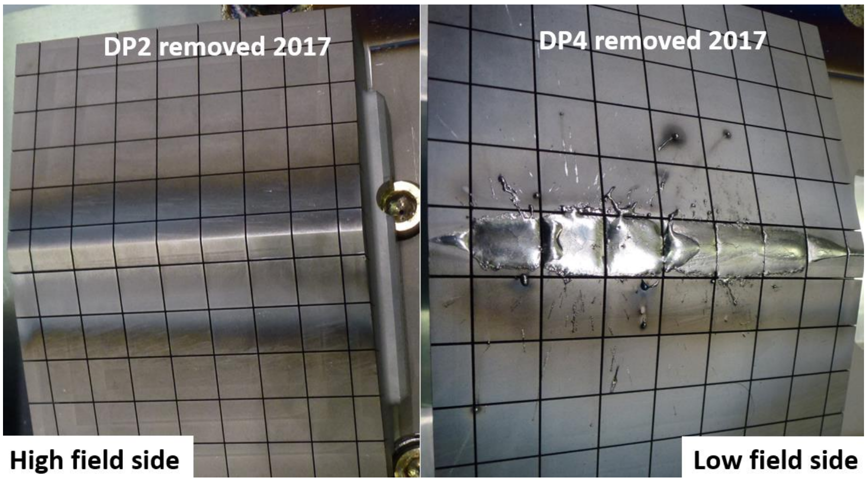

Figure 4 c

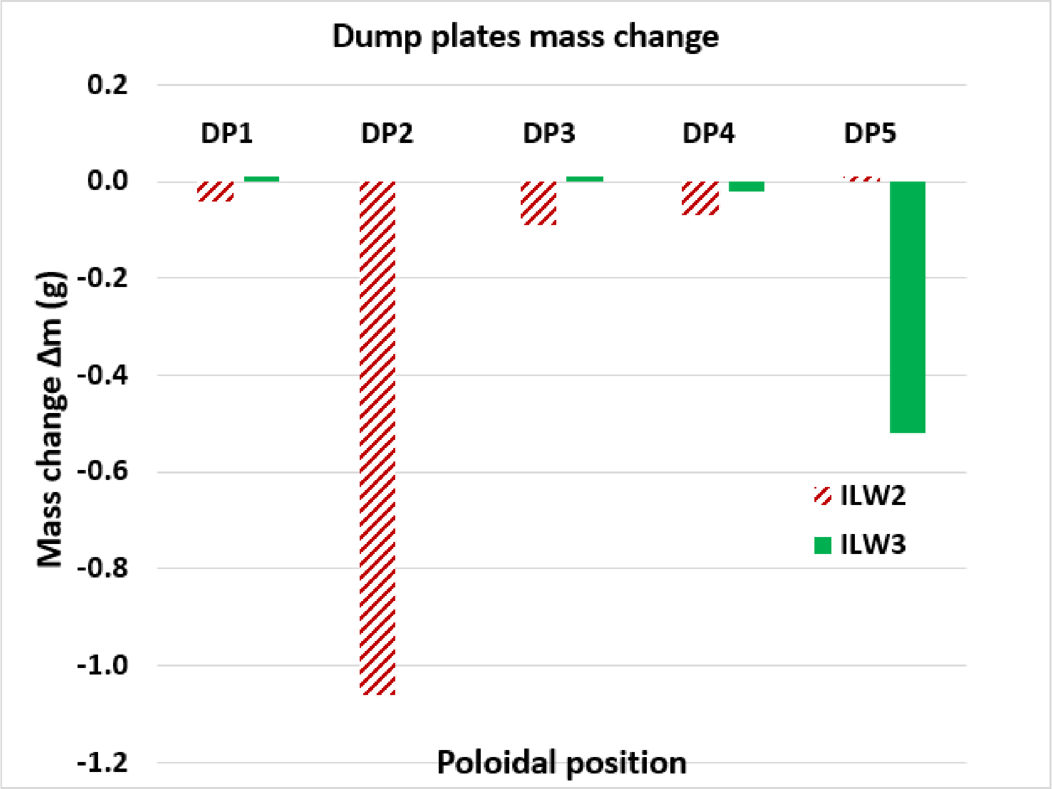

Figure 5

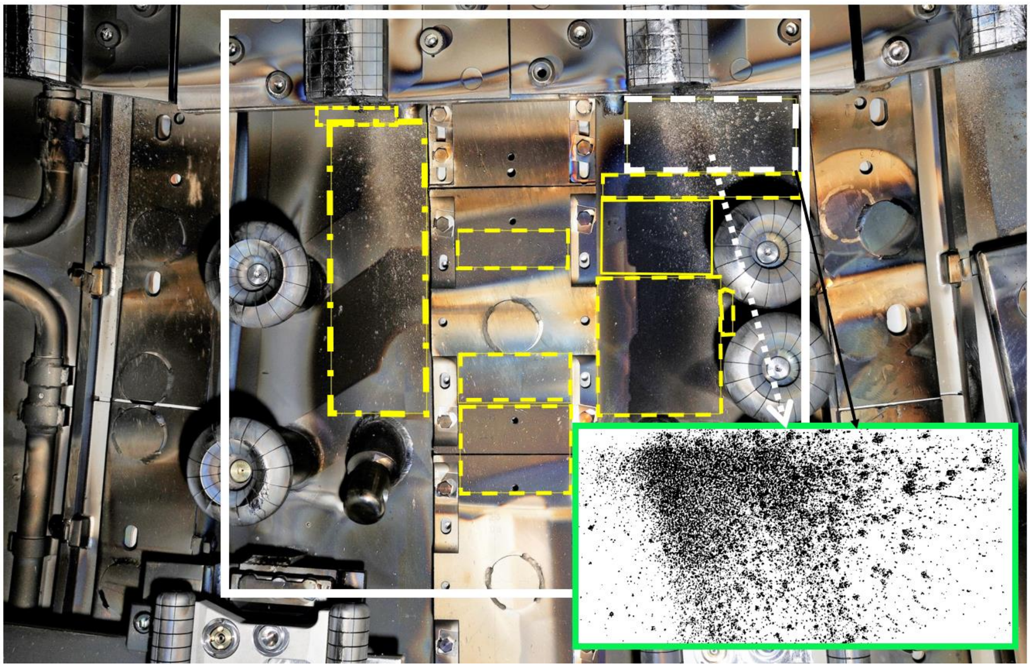

Figure 6

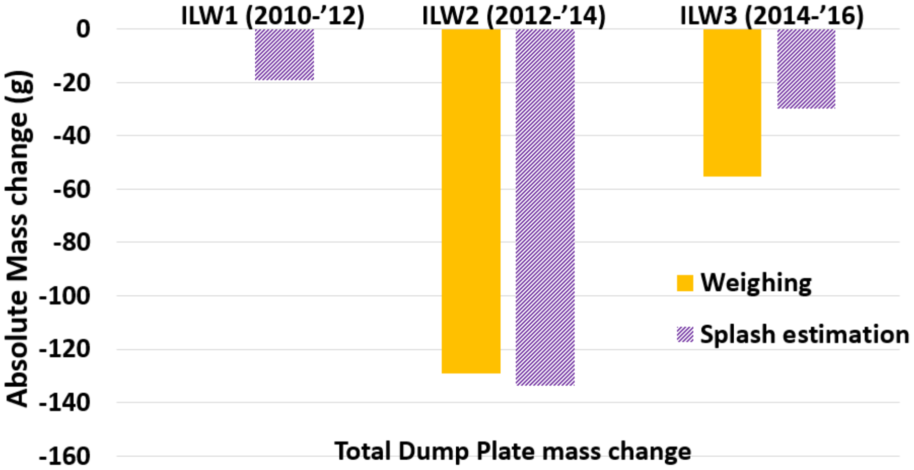

Figure 7

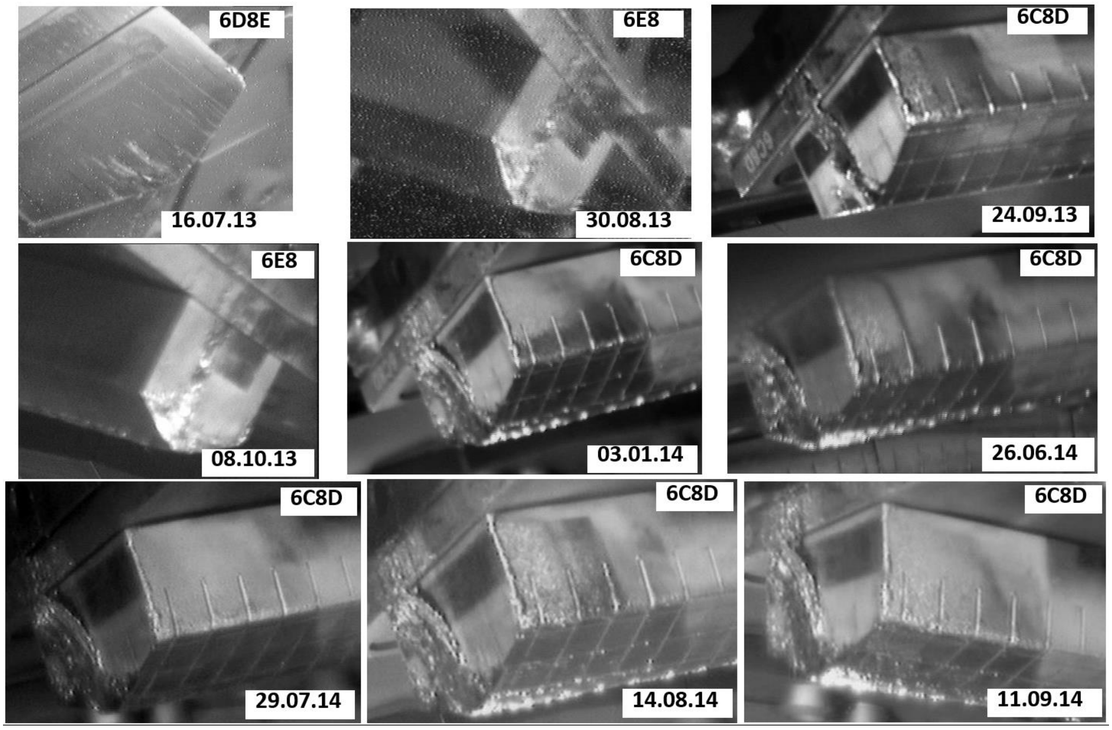

Figure 8

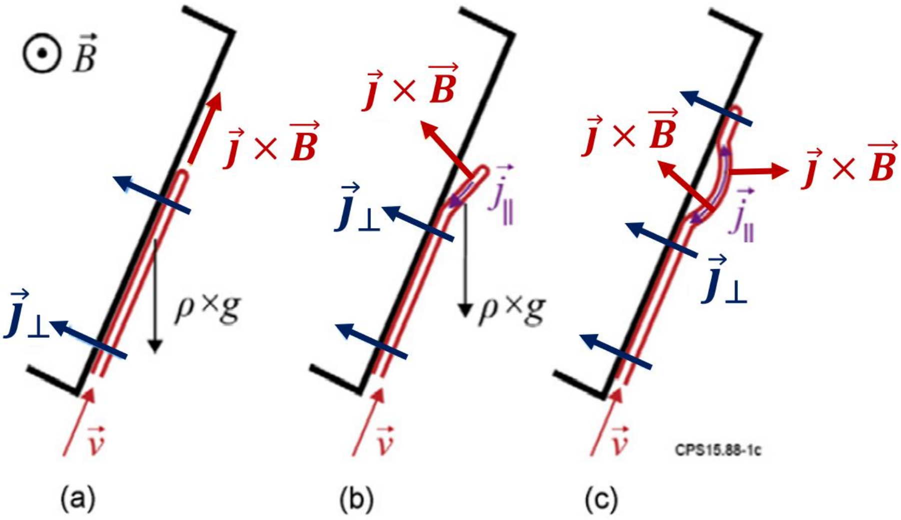

Figure 9 – reprint from [18]

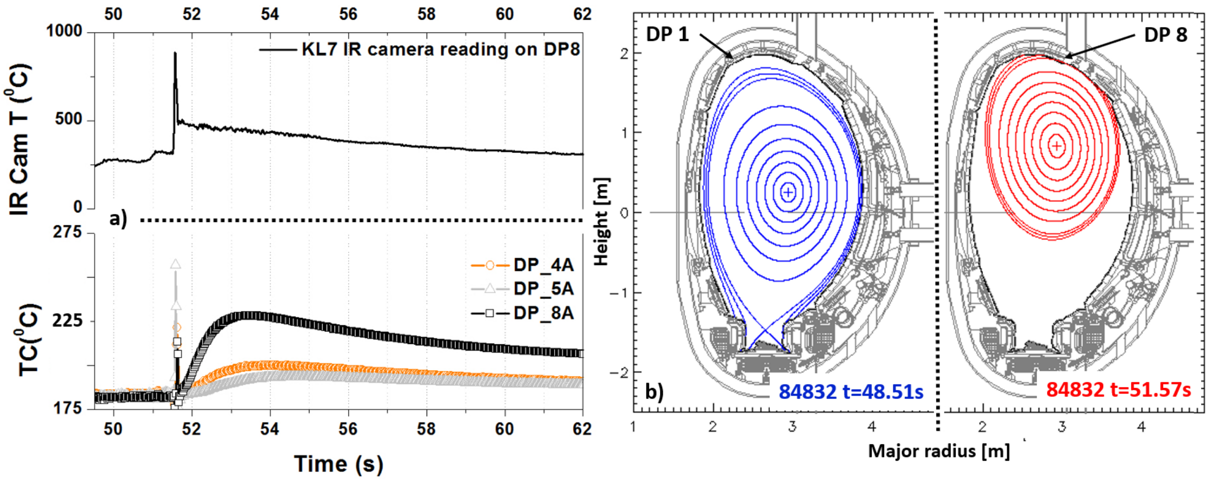

Figure 10

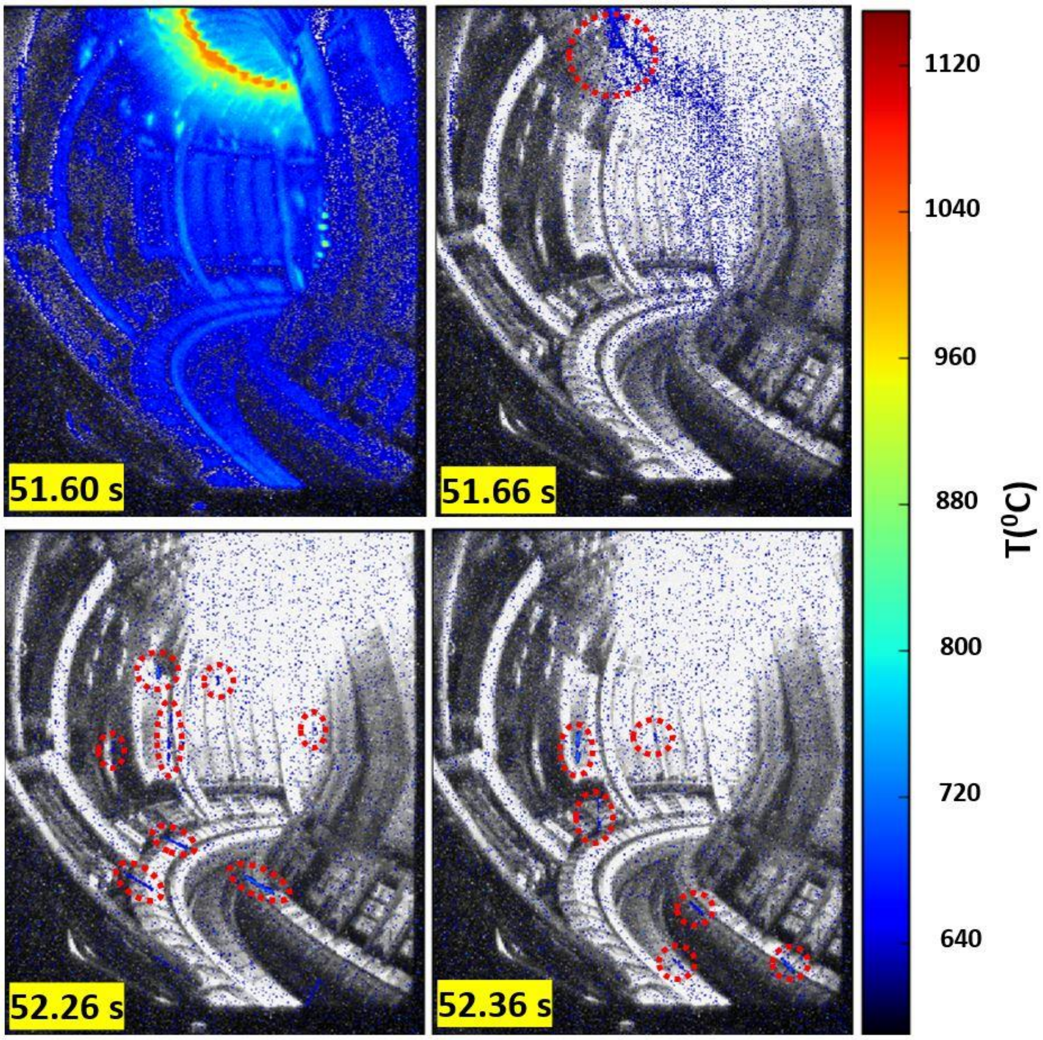

Figure 11

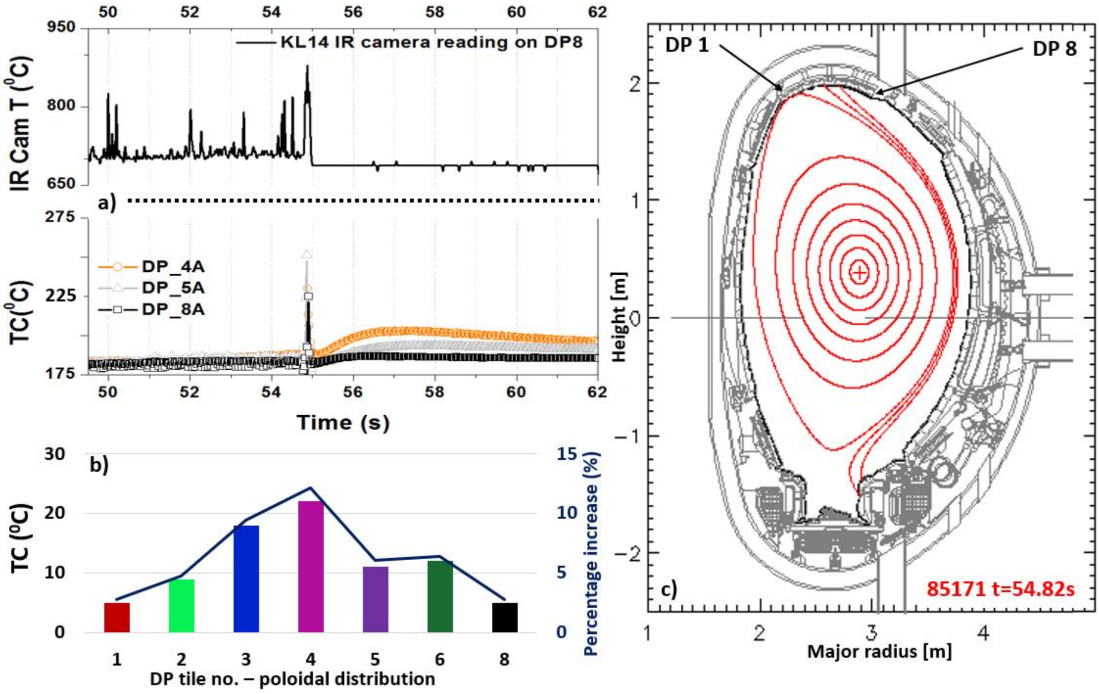

Figure 12

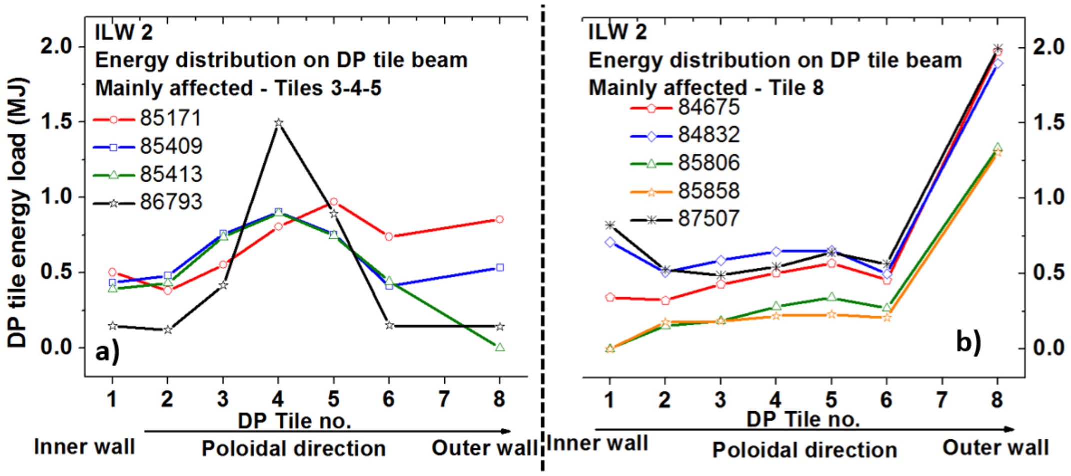

Figure 13

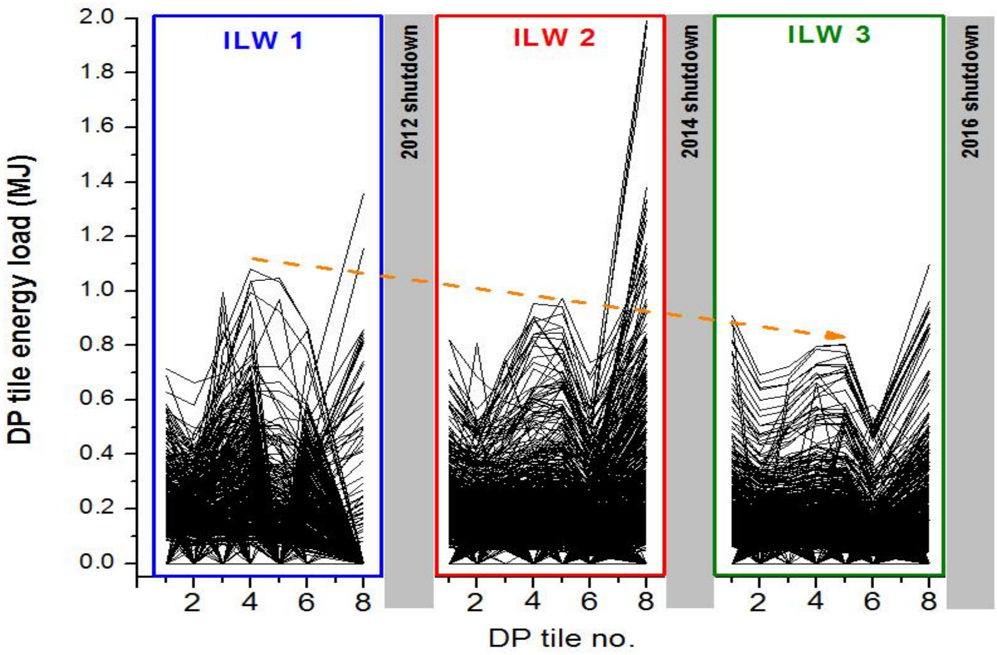

Figure 14

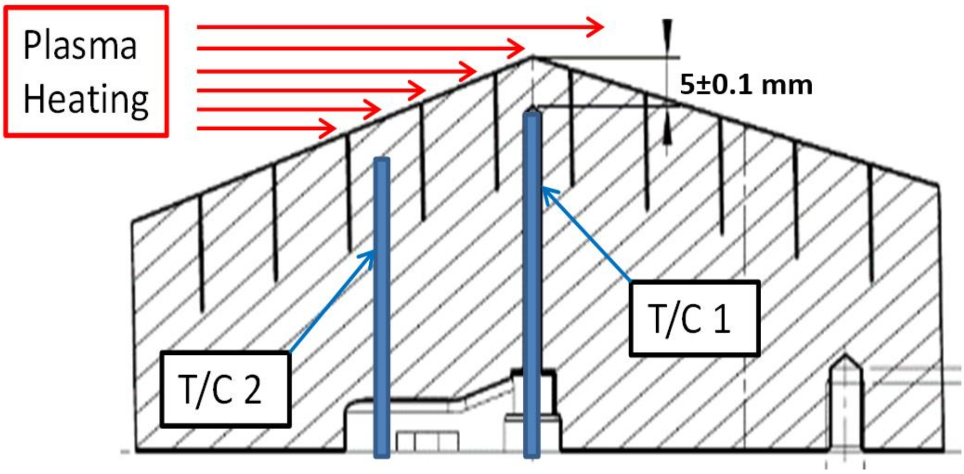

Figure 15

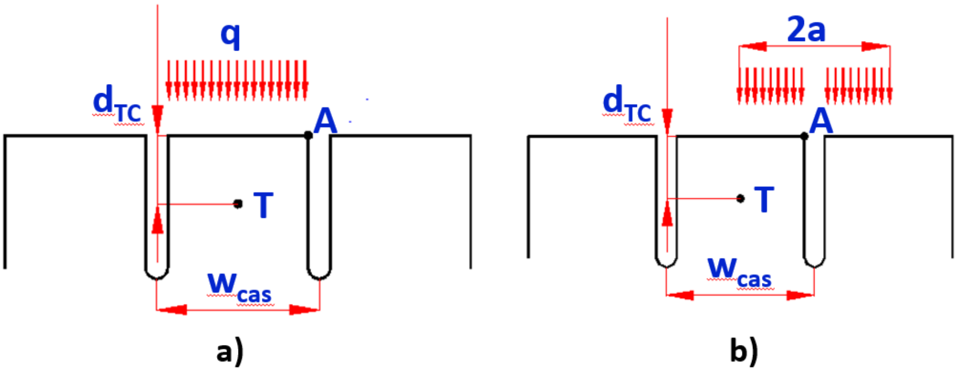

Figure 16

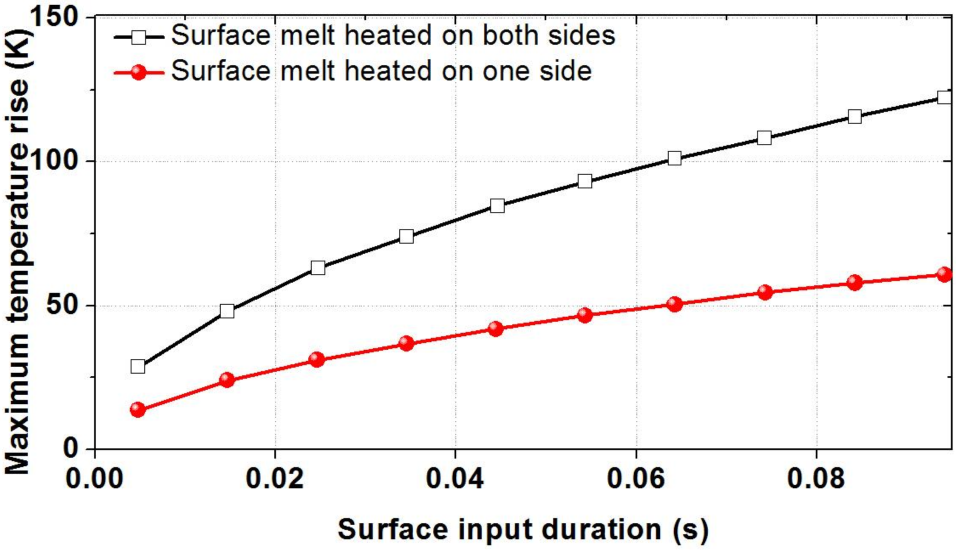

Figure 17

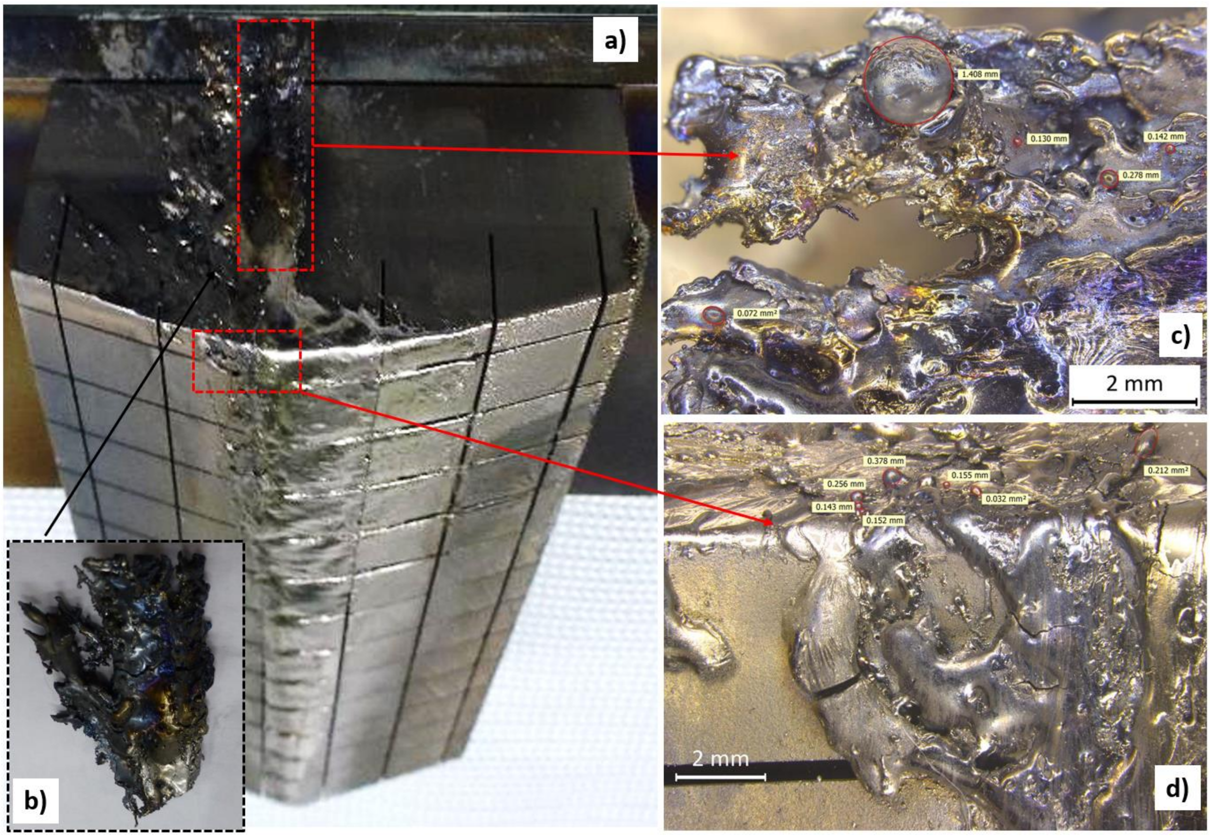

Figure 18

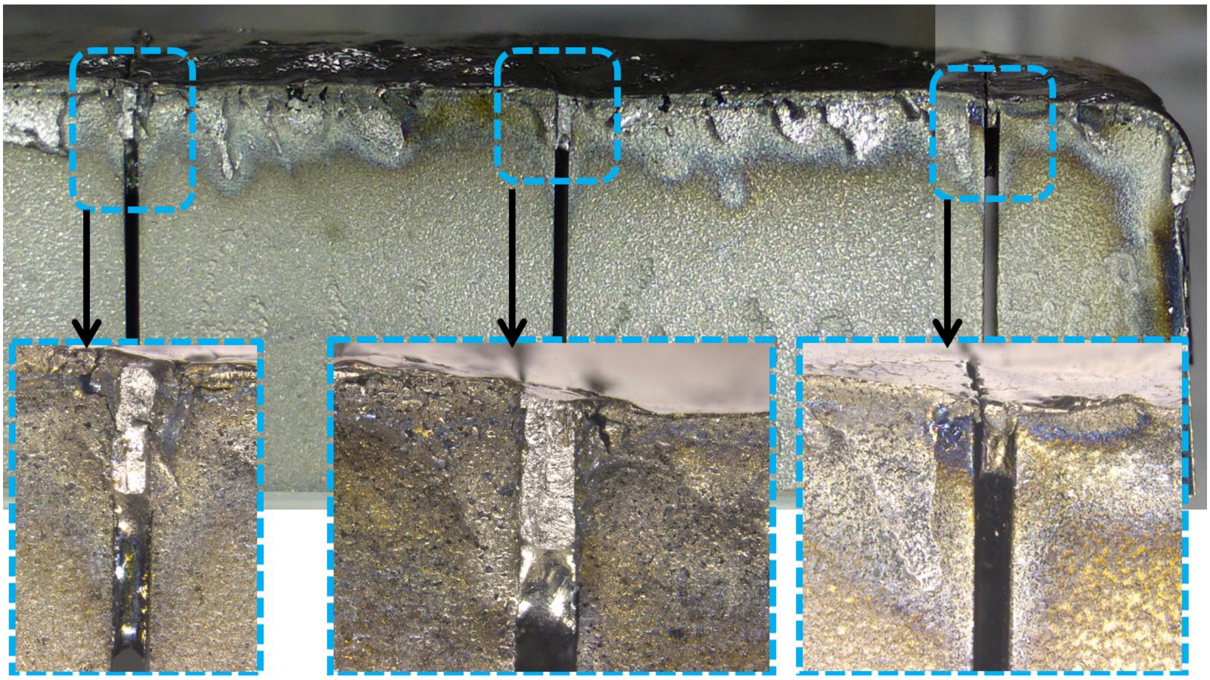

Figure 19

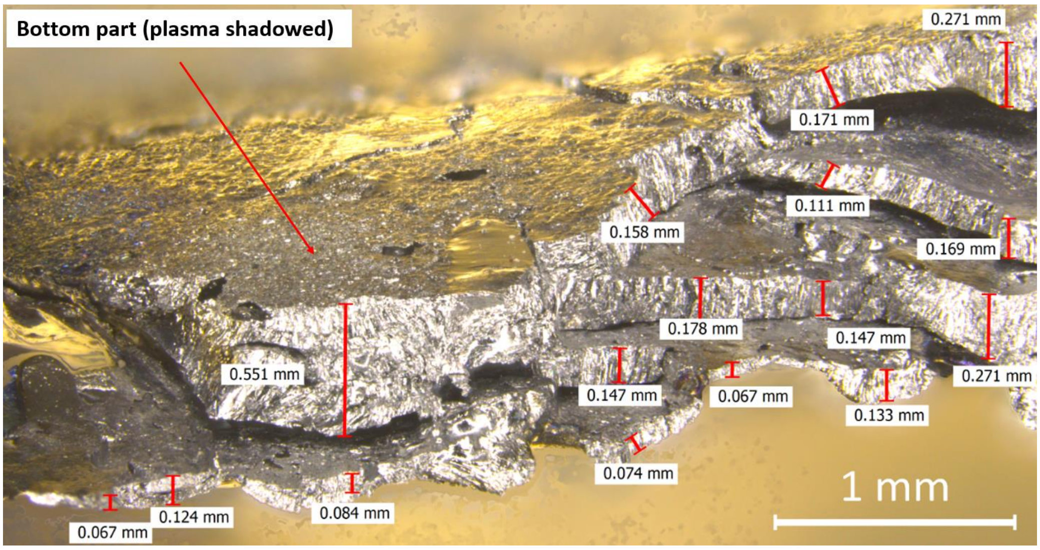

Figure 20

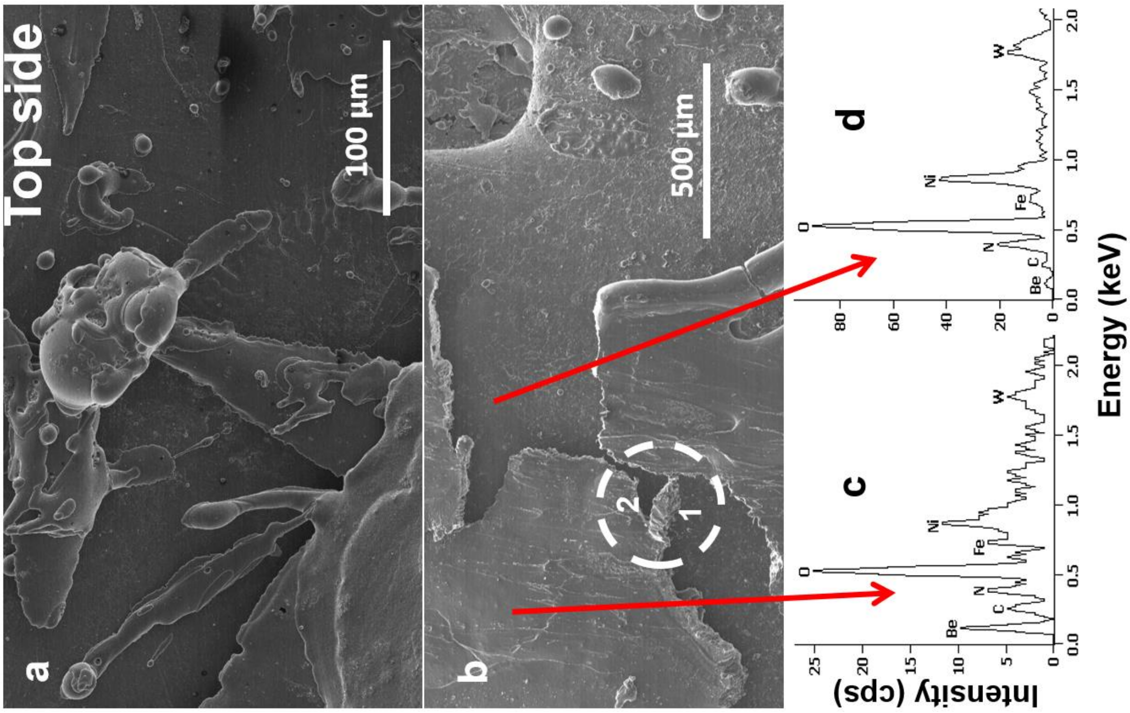

Figure 21

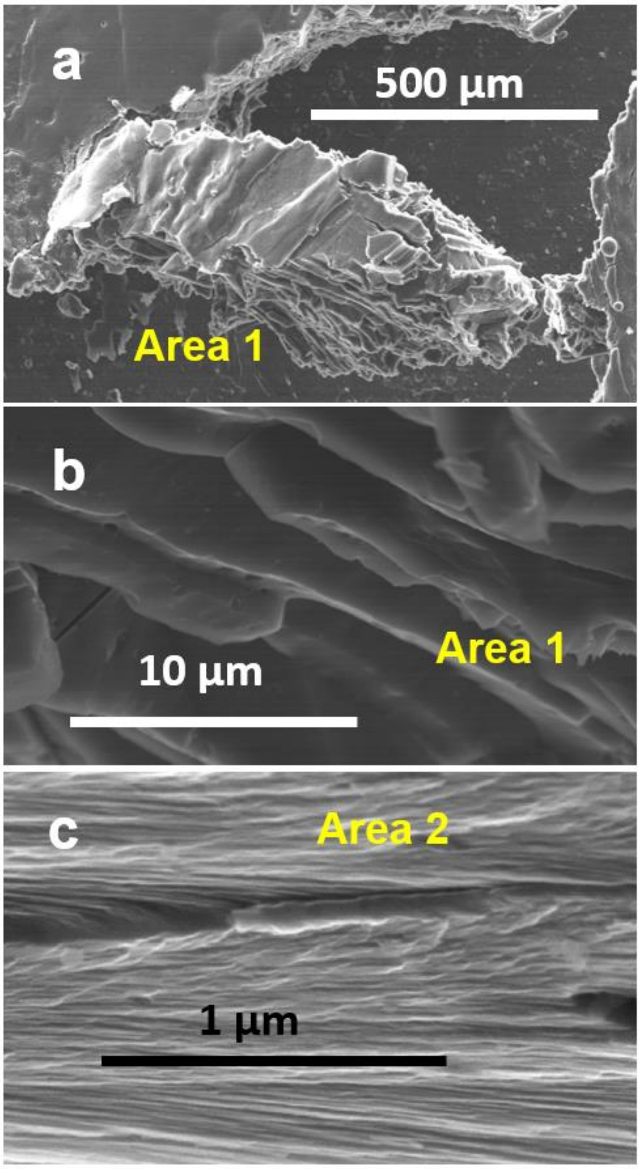

Figure 22

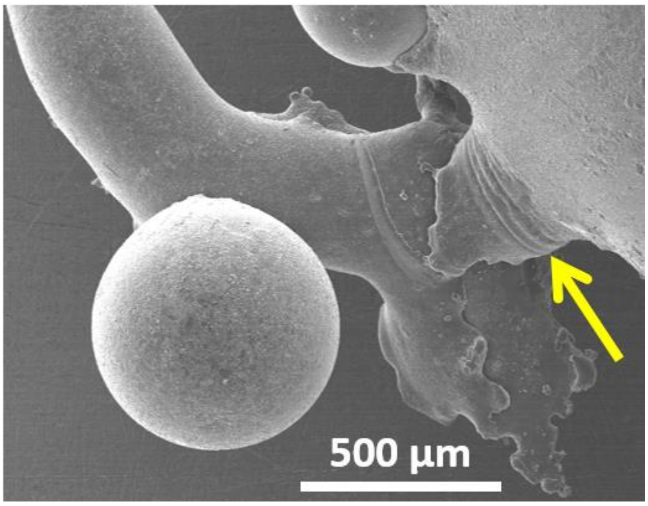

Figure 23

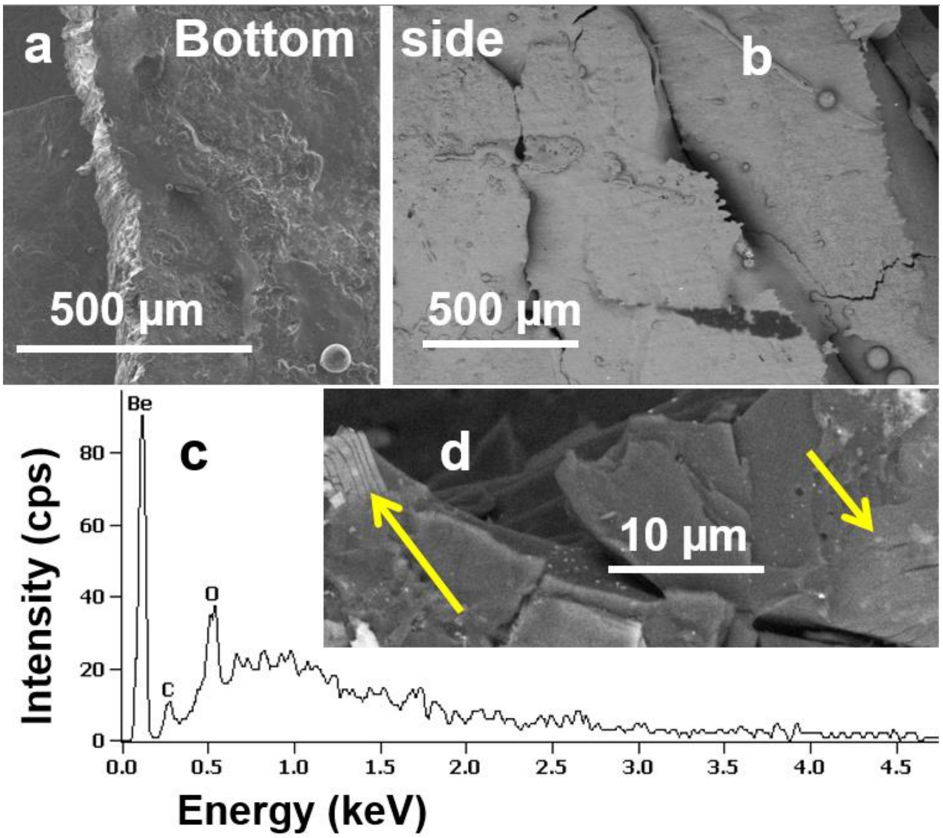

Figure 24

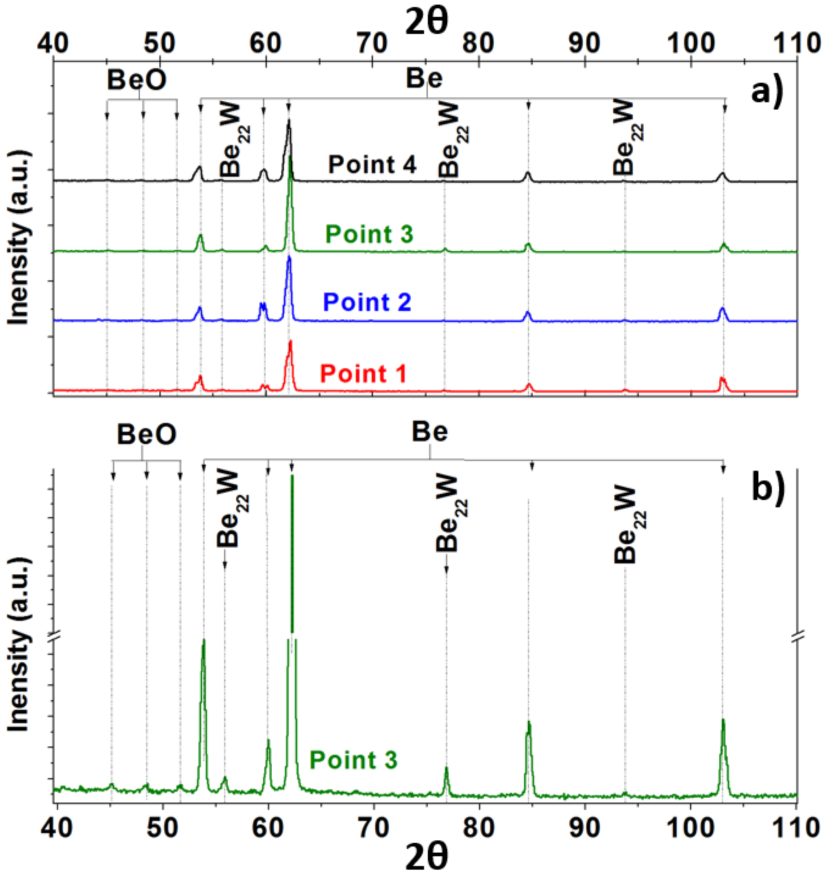

Figure 25

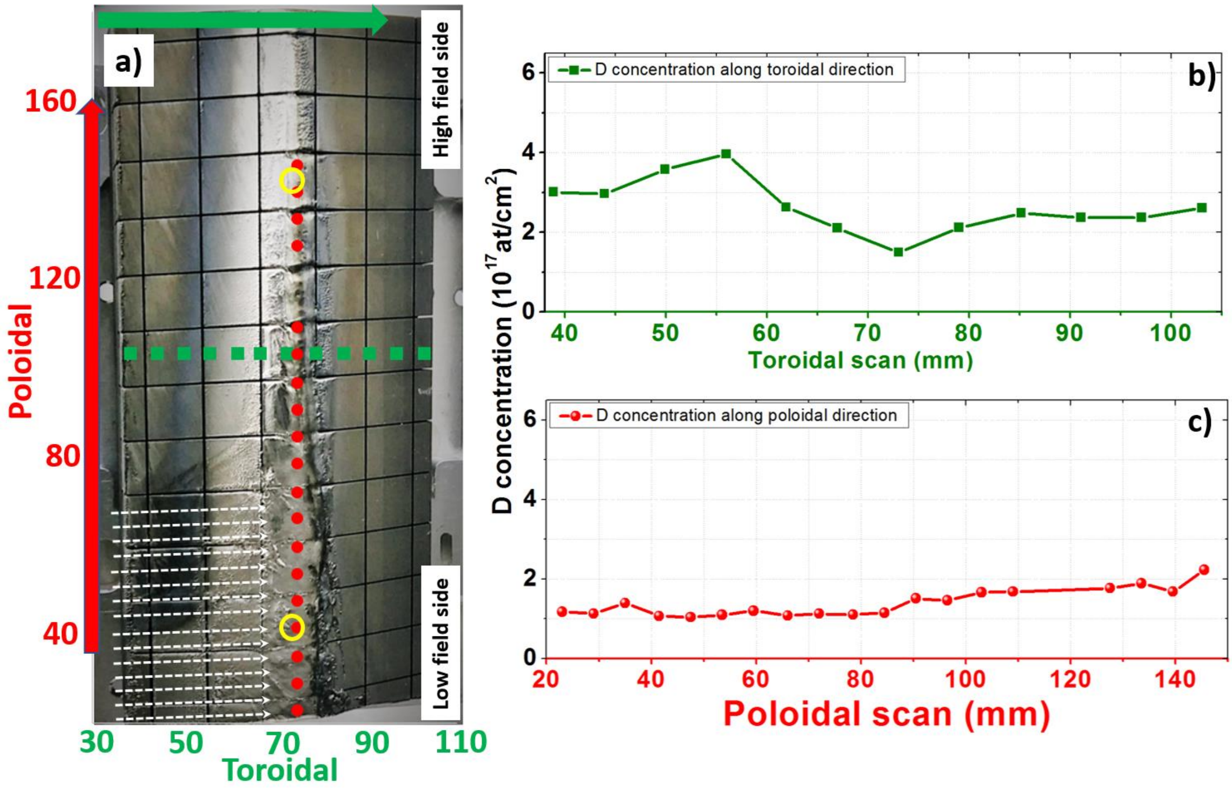

Figure 26

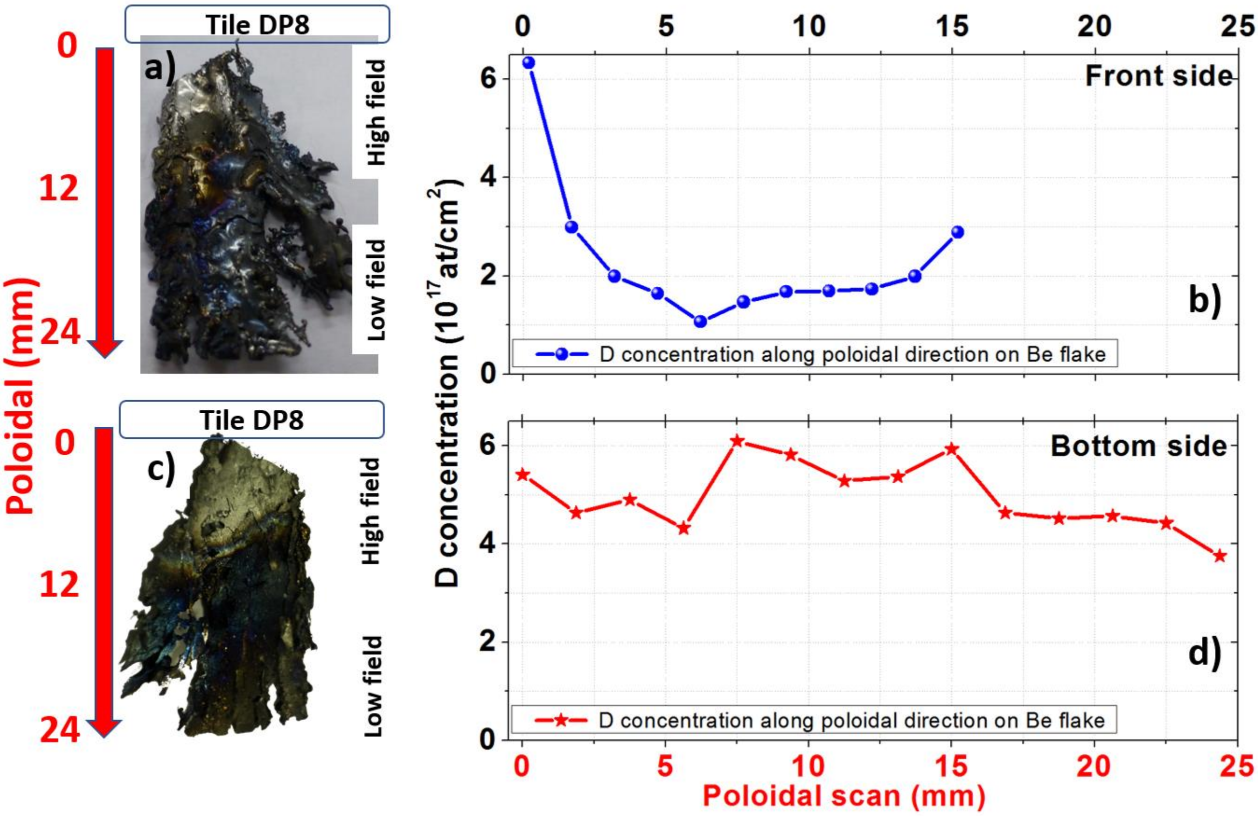

Figure 27